Fluid pressure diffusion effects on the seismic reflectivity of a single fracture

Nicolás D. Barbosa[a)]

Applied and Environmental Geophysics Group,

Institute of Earth Sciences,

University of Lausanne,

Lausanne,

Switzerland

J. Germán Rubino

Department of Earth Sciences,

University of Western Ontario,

London,

Ontario,

Canada

Eva Caspari, Marco Milani, and Klaus Holliger

Applied and Environmental Geophysics Group,

Institute of Earth Sciences,

University of Lausanne,

Switzerland

(Dated: September 14, 2016)

* Manuscript accepted for publication in J. Acoust. Soc. Am.

Abstract

When seismic waves travel through a fluid-saturated porous medium containing a fracture, fluid pressure gradients are induced between the compliant fracture and the stiffer embedding background. The resulting equilibration through fluid pressure diffusion (FPD) produces a frequency dependence of the stiffening effect of the fluid saturating the fracture. As the reflectivity of a fracture is mainly controlled by the stiffness contrast with respect to the background, these frequency-dependent effects are expected to affect the fracture reflectivity. We explore the P- and S-wave reflectivity of a fracture modelled as a thin porous layer separating two half-spaces. Assuming planar wave propagation and P-wave incidence, we analyze the FPD effects on the reflection coefficients through comparisons with a low-frequency approximation of the underlying poroelastic model and an elastic model based on Gassmann's equations. The results indicate that, while the impact of global flow on fracture reflectivity is rather small, FPD effects can be significant, especially for P-waves and low incidence angles. These effects get particularly strong for very thin and compliant, liquid-saturated fractures and embedded in a high-permeability background. In particular, this study suggests that in common environments and typical seismic experiments FPD effects can significantly increase the seismic visibility of fractures.

PACS numbers: 43.20.Gp, 43.20.Bi

I. INTRODUCTION

The presence of fractures is very common throughout the Earth's upper crust. As fractures are highly permeable and compliant, especially with respect to the embedding material, they tend to dominate the mechanical and hydraulic properties of the corresponding medium. For this reason, there is great interest in improving non-invasive techniques for detecting and characterizing fractures for a wide range of applications throughout the Earth, environmental, and engineering sciences. Seismic waves are widely employed for this purpose due to the fact that they are significantly attenuated and delayed and show strong anisotropy in presence of fractures (e.g., Gurevich et al., 2009; Müller et al., 2010; Rubino et al., 2014)

Despite the very large contrasts in scale typically observed between fracture apertures and prevailing seismic wavelengths, seismic imaging of extensive individual fractures is often possible and hence amenable to conventional interpretation approaches, such as, for example, amplitude-versus-offset analysis (e.g., Pirak-Nolte et al., 1990; Oelke et al., 2013; Minato and Ghose, 2014). Although this phenomenon is generally attributed to the high compliance of the fractures with respect to the background, the details of the underlying physics remain rather enigmatic. To date, this problem has been mostly addressed based on the so-called linear slip theory, where a fracture is modelled as an interface and its effect is represented by a discontinuity in displacement assuming continuous traction across the interface. The jump in the displacement vector is linearly related to the traction vector through a compliance matrix (Schoenberg, 1980; Pirak-Nolte et al., 1990). When the compliance matrix is real-valued, the model represents a long-wavelength approximation of an elastic thin-layer model (Li et al., 2014). Worthington and Lubbe (2007) provide a summary of real-valued normal and shear fracture compliances for fluid-filled fractures as functions of the fracture size, obtained from seismic and laboratory experiments. Oelke et al. (2013) model individual fractures as thin fluid layers embedded in an elastic background and derive the corresponding elastic compliances to be used in a framework based on the linear slip model.

[a] Electronic address: Nicolas.Barbosa@unil.ch

However, when a seismic wave travels through a fluid-saturated porous rock containing an open fracture, the wave will perturb the fluid pressure equilibrium in the pore space because the fracture is much softer than the embedding background. Consequently, fluid pressure diffusion (FPD) is induced between the fracture and the background in order to return the state of equilibrium. This can affect significantly the stiffening effect of the saturating pore fluid in the fracture, thus changing the compressibility contrast with respect to the background and, therefore, the fracture reflectivity. Moreover, the acceleration of the rock matrix produced by a passing seismic wave field, together with the fluid pressure gradient established between its peaks and troughs, generates an additional perturbation of the fluid displacement field. This is commonly referred to as global flow and can also affect the seismic response of the fracture. These fluid-flow-related effects cannot be accounted for in a purely elastic framework, which inherently assumes that no flow occurs across the fracture interfaces. The linear slip model also struggles with considering these effects as it represents the fracture as an interface separating two non-porous media. A recent effort to alleviate this problem was made by Rubino et al. (2015), who developed a model for including FPD effects in the framework of the linear slip theory by considering frequency-dependent and complex-valued normal compliances. These authors considered a 1D system composed of a large number of regularly distributed planar fractures with a separation much smaller than the prevailing seismic wavelength.

To date, the study of the effects of global flow and FPD between background and fracture on the seismic reflectivity of a single fracture remains rather unexplored. One of the few works related with this topic was carried out by Gurevich et al. (1994). Using the low-frequency approximation of Biot's (1962) theory and considering normal-incidence and relatively mild contrasts between a thin layer and the embedding background, they found that FPD effects are significant only for very low frequencies, for which the reflectivity of the thin layer is rather negligible. However, the conclusions of Gurevich et al. (1994) cannot be extended to the case of fractured rocks, as in this case very large contrasts in the rock physical properties are expected. More recently and also in a poroelastic context, Nakagawa and Schoenberg (2007) developed seismic boundary conditions across a single fracture and found that its scattering behavior is controlled by a set of characteristic parameters similar to those used in the classic linear slip theory. They focused their analysis on how the fluid pressure within a fracture affects its scattering behavior as a function of fracture permeability and pore fluid properties.

Here, we generalize the analysis of Gurevich et al. (1994) for arbitrary incidence angles and pronounced contrasts in the material properties characteristic of fractures. We also investigate the influence of Biot's global flow on the fracture reflections coefficients. We consider three thin-layer models to isolate and explore the fluid-flow-related effects, and perform an exhaustive sensitivity analysis to determine under which conditions these effects can affect significantly the reflectivity of a fracture.

The paper is organized as follows: First, we outline the plane-wave theory for thin-layer models (II A, B, C plus Appendices A, B, C) and present the pertinent frequency regimes that the effective fracture compliance experiences when poroelastic effects are considered (II D). Next, we provide an analysis of the conditions under which the stiffening effect of the fluid saturating the fracture is dominated by fluid pressure diffusion between the fracture and background (III). Finally, we study the sensitivity of fluid pressure diffusion effects to different pore fluids saturating the fracture, background permeability, fracture and background dry-frame stiffness, and fracture aperture (IV).

II. METHODOLOGY

To study fluid-flow-related effects on the reflectivity of a single fracture, we utilize three thin-layer models: First, a poroelastic thin-layer model in the context of Biot's (1962) theory; second, a low-frequency approximation of the poroelastic model; and, lastly, an elastic thin-layer model using Gassmann's (1951) equations to define the parameters of the background and fracture. The comparison between the seismic responses obtained based on these models allows us to explore the physical processes related to wave-induced FPD as well as to global flow, and to assess the conditions under which these effects have a significant impact on the reflectivity of an individual fracture.

A. Full poroelastic model

When a seismic wave strikes a fracture, fluid flow is induced across its interfaces in response to (i) the spatial gradient in fluid pressure created between the fracture and background due to their differing compressibilities (mesoscopic flow), and (ii) to the combined effect of the fluid pressure gradients prevailing between peaks and troughs of the seismic wave and the accelerations induced by the passing wavefield (global flow). In order to take into account these effects on the reflectivity of a single fracture, we compute the reflection coefficients in the framework of the theory of poroelasticity (Biot, 1962).

Following Nakagawa and Schoenberg (2007), we conceptualize the fracture as a highly compliant and highly porous thin layer embedded in a much stiffer and much less porous background. To this end, we consider two half-spaces Ω_1 and Ω_3 embedding a thin layer Ω_2 of thickness h representing the fracture (Fig. 1). We assume each medium to consist of a solid, elastic, homogeneous and isotropic skeleton containing fully fluid-saturated pores. Therefore, the governing physical properties are the porosity ϕ, the dry frame bulk modulus K_m, the dry frame shear modulus μ_m, the static permeability κ, the grain density ρ_s, the grain bulk modulus K_s, the fluid bulk modulus K_f, the fluid density ρ_f, and the fluid viscosity η. The shear modulus and bulk density of the saturated rock are

$$\begin{aligned} \mu &= \mu_m, \\ \rho_b &= (1-\phi)\rho_s + \phi\rho_f. \end{aligned} \tag{1}$$

It is important to emphasize that representing the fracture as a thin poroelastic layer is just one of many possible models used to study seismic response of fractures. Nevertheless, many authors have investigated and discussed the conditions under which a thin-layer model with appropriate material infill can be thought of as an equivalent representation of more realistic fracture models in porous rocks (e.g., Hudson and Liu, 1999; Rubino et al., 2014).

For this study, we consider an incident fast P-wave and thus, using the Cartesian coordinate system shown in Fig. 1, it is sufficient to study the wave propagation in the x-y plane as, in this case, there is no wave propagation in the z-direction. In space-frequency domain, let $\mathbf{u} = \mathbf{u}(\mathbf{x}, \omega)$ be the average displacement of the solid phase, $\tilde{\mathbf{u}} = \tilde{\mathbf{u}}(\mathbf{x}, \omega)$ the average displacement of the fluid phase and $\mathbf{w} = \mathbf{w}(\mathbf{x}, \omega) = \phi(\tilde{\mathbf{u}}(\mathbf{x}, \omega) - \mathbf{u}(\mathbf{x}, \omega))$ the average relative displacement of the fluid phase with $\mathbf{x} = (x, y)$ being the position vector in $\mathbb{R}^2$ and ω the angular frequency. With τ_{ij} and p_f denoting the total stress tensor and the fluid pressure, the isotropic constitutive relations for poroelastic media are (Biot, 1962)

$$\begin{aligned} \tau_{ij}(\mathbf{u}, \mathbf{w}) &= 2\mu\varepsilon_{ij} + \delta_{ij}(\lambda \nabla \cdot \mathbf{u} + \alpha M \nabla \cdot \mathbf{w}), \\ p_f(\mathbf{u}, \mathbf{w}) &= -\alpha M \nabla \cdot \mathbf{u} - M \nabla \cdot \mathbf{w}, \qquad i, j = x, y, \end{aligned} \tag{2}$$

where $\varepsilon_{ij} = \frac{1}{2}(\frac{\partial u_i}{\partial x_j} + \frac{\partial u_j}{\partial x_i})$ is the strain tensor and $\lambda = K_m - \frac{2}{3}\mu + \alpha^2 M$ is the Lamé constant. The Biot-Willis effective stress coefficient α and the Biot's fluid-storage modulus M are equal to (Dutta and Ode, 1983)

$$\begin{aligned} \alpha &= 1 - K_m/K_s, \\ M &= \left(\frac{\alpha - \phi}{K_s} + \frac{\phi}{K_f} \right)^{-1}. \end{aligned} \tag{3}$$

Then, the dynamic equations for an isotropic, homogeneous medium stated in the space-frequency domain can be written as (Biot, 1962)

$$\begin{aligned} -\omega^2 \rho_b \mathbf{u} - \omega^2 \rho_f \mathbf{w} &= H_U \nabla(\nabla \cdot \mathbf{u}) + \alpha M \nabla(\nabla \cdot \mathbf{w}) - \mu \nabla \times (\nabla \times \mathbf{u}), \\ -\omega^2 \rho_f \mathbf{u} - \omega^2 g(\omega) \mathbf{w} + i\omega b(\omega) \mathbf{w} &= \alpha M \nabla(\nabla \cdot \mathbf{u}) + M \nabla(\nabla \cdot \mathbf{w}), \end{aligned} \tag{4}$$

where $b(\omega)$ and $g(\omega)$ are the viscous and mass coupling coefficients, respectively (Appendix A), whereas $H_U = \lambda + 2\mu$ is the undrained P-wave modulus. By performing a plane-wave analysis, it can be shown that Biot's theory supports the propagation of one S-wave and two P-waves. The fast P- and S-waves correspond to the classical longitudinal and transversal waves propagating in elastic or viscoelastic isotropic solids. The additional slow P-wave, which is due to the presence of a fluid phase in the pore space, is a fluid pressure diffusion at low frequencies and a propagating wave at high frequencies. Biot's characteristic frequency separates the low-frequency regime, where the relative fluid displacement is governed by the viscous forces, from the high-frequency regime, where the inertial forces dominate (Johnson et al., 1987). It is possible to express this frequency as

$$\omega_B = 2\pi f_B = \frac{\eta\phi}{\rho_f \kappa S}, \tag{5}$$

where S is the tortuosity of the rock.

We consider an incident plane fast P-wave, denoted by the superscript I, of frequency ω propagating in the x-y plane and arriving from Ω_1 at the interface Γ_1 (y=0) between Ω_1 and Ω_2 (Fig. 1). θ^I is the angle of incidence with respect to the normal to Γ_1. The energy

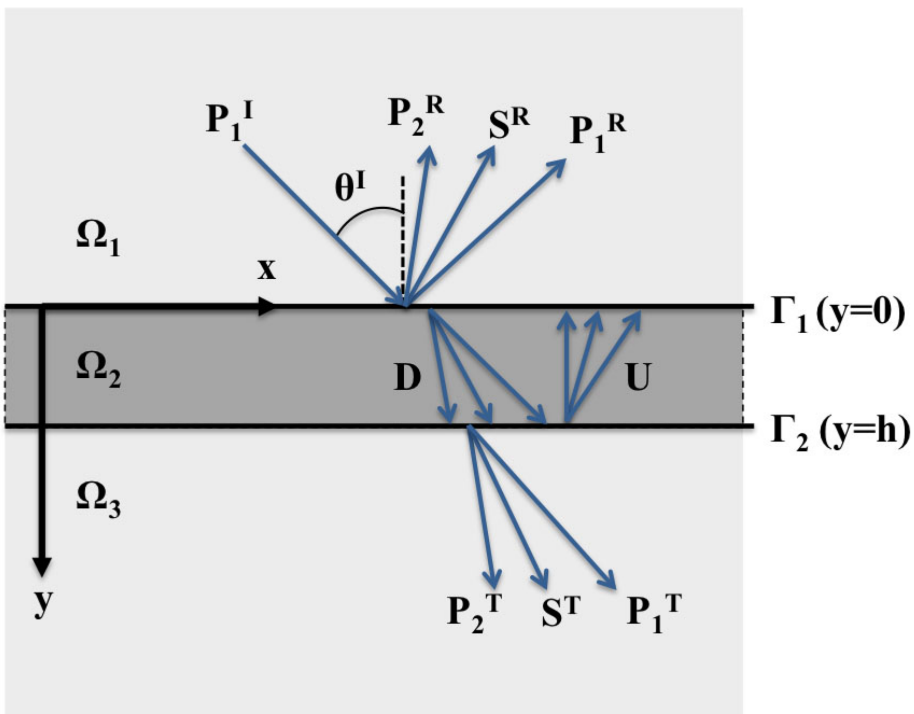

FIG. 1. (Color Online) Schematic illustration of the seismic model considered. The arrows indicate the positive directions of wave propagation. P_1, P_2 and S refer to the fast and slow compressional and shear waves, respectively. The superscripts R, T, D and U denote the reflected waves in Ω_1, transmitted waves in Ω_3 and downgoing and upgoing wave fields inside the fracture, respectively.

of the incident wave is thus, split into two compressional waves and one shear wave in Ω_1, denoted by the superscript R, in Ω_3, denoted by the superscript T, and six wave modes in the layer Ω_2 (Fig. 1). In the latter case, there are two shear, two fast compressional and two slow compressional upgoing and downgoing waves denoted by superscripts U and D, respectively. Therefore, following the superposition principle, the displacement vectors in each domain Ω_i are given by

$$\begin{aligned}
\mathbf{u}^{\Omega_1} &= \mathbf{u}^I_{P_1} + \sum_j \mathbf{u}^R_j, & \mathbf{w}^{\Omega_1} &= \mathbf{w}^I_{P_1} + \sum_j \mathbf{w}^R_j, \\
\mathbf{u}^{\Omega_2} &= \sum_j \left(\mathbf{u}^U_j + \mathbf{u}^D_j\right), & \mathbf{w}^{\Omega_2} &= \sum_j \left(\mathbf{w}^U_j + \mathbf{w}^D_j\right), \\
\mathbf{u}^{\Omega_3} &= \sum_j \mathbf{u}^T_j, & \mathbf{w}^{\Omega_3} &= \sum_j \mathbf{w}^T_j, \qquad j = P_1, P_2, S.
\end{aligned} \tag{6}$$

As we consider plane waves, the compressional wave modes for the solid and relative fluid displacements can be computed from scalar potentials in the form (Dutta and Ode, 1983)

$$\begin{aligned}
&\mathbf{u}^q_j(\mathbf{x}, \omega) = \nabla \Phi^q_j, \\
&\mathbf{w}^q_j(\mathbf{x}, \omega) = \nabla \tilde{\Phi}^q_j, \qquad j = P_1, P_2, \text{ and } q = I, R, U, D, T.
\end{aligned} \tag{7}$$

The corresponding scalar potentials are

$$\Phi^q_j = A^q_j e^{i(\omega t - \mathbf{k}^q_j \cdot \mathbf{x})} \ , \ \tilde{\Phi}^q_j = B^q_j e^{i(\omega t - \mathbf{k}^q_j \cdot \mathbf{x})}, \tag{8}$$

where i is the imaginary unit, t is the time, and

$$\mathbf{k}^q_j = (n^q_j, l^q_j), \tag{9}$$

denotes the corresponding complex wave vector with horizontal and vertical components n^q_j and l^q_j, respectively. We assume homogeneous incident fast P-wave and thus,

$$\mathbf{k}^I_{P_1} = k^I_{P_1}(sin(\theta^I), cos(\theta^I)), \tag{10}$$

where $k^I_{P_1}$ is the complex fast P-wavenumber. The wave vectors derive from solving Eqs. 4 in the corresponding medium (Appendix A). According to Eq. 8, the sign of the vertical component of the real part of $\mathbf{k}^q_j$ is positive for waves traveling in the direction of increasing y.

For rotational waves, vector potentials are employed and thus, the shear components of the displacements are given by

$$
\begin{aligned}
\mathbf{u}_S^q(\mathbf{x},\omega) &= -\nabla \times \Psi_s^q, \\
\mathbf{w}_S^q(\mathbf{x},\omega) &= -\nabla \times \tilde{\Psi}_s^q, \quad q = R, U, D, T.
\end{aligned}
\tag{11}
$$

The vector potentials are

$$
\Psi_s^q = A_s^q e^{i(\omega t - \mathbf{k}_s^q \cdot \mathbf{x})} \breve{e}_z \ , \ \ \tilde{\Psi}_s^q = B_s^q e^{i(\omega t - \mathbf{k}_s^q \cdot \mathbf{x})} \breve{e}_z, \tag{12}
$$

where $\breve{e}_z$ is the unit vector normal to the x-y plane and

$$
\mathbf{k}_S^q = (n_s^q, l_s^q), \tag{13}
$$

is the complex S-wave vector with the convention of signs described before.

Next, substituting Eqs. 7 and 11 in Eq. 6 we obtain the solid and relative fluid displacements in each medium Ω_i and, using the constitutive relations given by Eq. 2, the fluid pressure and total stress tensor can also be written as functions of the potential amplitudes. In order to obtain the amplitudes A_j^q and B_j^q for the different wave modes in the two half-spaces and the fracture, we impose the continuity of the solid particle displacement (u_x and u_y), the normal component of relative fluid displacement (w_y), the normal and tangential components of total stress (τ_{yy} and τ_{xy}), and the fluid pressure (p_f) across the interfaces Γ_1 and Γ_2 (Gurevich and Schoenberg, 1999). The considered open-pore conditions (continuity of p_f) at the interfaces allow for fluid exchange between the domains and are consistent with the validity of Biot's equations of poroelasticity at the interfaces. This set of boundary conditions leads to a linear system of equations with 12 unknowns whose solution provides the wave amplitudes (Appendix B).

Once we have obtained the amplitudes, the displacement reflection coefficients can be defined as the ratio of the solid displacement magnitude of the corresponding reflected wave and that of the incidence wave on Γ_1 (e.g., Rubino et al., 2006)

$$\begin{aligned} R_{P_1P_1} &= \frac{|\mathbf{u}^R_{P_1}|}{|\mathbf{u}^I_{P_1}|} = \frac{A^R_{P_1}}{A^I_{P_1}}, \\ R_{P_1P_2} &= \frac{|\mathbf{u}^R_{P_2}|}{|\mathbf{u}^I_{P_1}|} = \frac{A^R_{P_2}k^R_{P_2}}{A^I_{P_1}k^I_{P_1}}, \\ R_{P_1S} &= \frac{|\mathbf{u}^R_{S}|}{|\mathbf{u}^I_{P_1}|} = \frac{A^R_{S}k^R_{S}}{A^I_{P_1}k^I_{P_1}}. \end{aligned} \tag{14}$$

It is important to mention that these reflection coefficients are complex-valued. We limit the analysis to reflection coefficients as transmission coefficients do not provide any additional insight.

B. Low-frequency poroelastic model

Here, we present a low-frequency poroelastic approach that aims at modelling the reflectivity considering only the mesoscopic FPD effects between the fracture and the background. That is, we neglect global flow effects. To this end, we compute the reflection coefficients in a similar fashion as for the full poroelastic model but using the low-frequency approximation of Biot's equations. As shown by Gurevich et al. (1994), this can be done by considering the following wavenumbers

$$\begin{aligned} k_{P_1} &= \frac{\omega}{V_P}, \\ k_S &= \frac{\omega}{V_S}, \\ k_{P_2} &= \frac{\sqrt{i}}{L_D}, \end{aligned} \tag{15}$$

where V_P and V_S are the low-frequency limits of the fast P- and S-waves velocities (Appendix A). The diffusion length in the equation of the slow P-wavenumber is

$$L_D = \sqrt{\frac{D}{\omega}}, \tag{16}$$

being $D = \frac{\kappa N}{\eta}$ the diffusivity of the medium and $N = \left(M - \frac{\alpha^2 M^2}{H_U}\right)$. In this low-frequency poroelastic approach, regardless the frequencies considered, the slow P-wave behaves as a diffusive mode. Moreover, for frequencies lower than Biot's characteristic frequency ω_B, the full solution and the low-frequency approximation are expected to be similar.

C. Elastic model

In order to assess fluid flow effects on the reflection coefficient of a fracture, the same procedure described for porous media was adopted in the framework of elastic media. For this model, the material properties of each medium are defined using Gassmann's (1951) equation. By doing so, the fluid pressure is assumed to be in equilibrium in each domain and the boundaries between the fracture and background are sealed.

For a purely elastic model, the seismic response is fully described by a single solid displacement field and the constitutive relation is given by Hooke's law

$$\tau_{ij}(\mathbf{u}) = 2\mu\varepsilon_{ij} + \delta_{ij}\lambda\nabla\cdot\mathbf{u} \qquad \text{for } i,j = x,y. \tag{17}$$

The natural boundary conditions for this model are the continuity of the solid displacement and of the normal and tangential components of the stress field at each interface. Proceeding in a similar fashion as for the previous models, we get an 8×8 linear system of equations whose solution provides the potential amplitudes for the compressional and shear waves. The definition of the reflection coefficients R_{PP} and R_{PS} is the same as for poroelastic media.

This model is expected to provide the same seismic response as both poroelastic models at frequencies which are lower than Biot's characteristic frequency ω_B but high enough to cause the fracture to behave in an *undrained* manner with respect to mesoscopic FPD. That is, the interfaces Γ_1 and Γ_2 behave as being sealed with respect to fluid pressure communication.

D. Frequency regimes

Müller and Rothert (2006) showed that for $\omega < \omega_B$, the frequency dependence of the effective stiffness of a periodically layered medium has three distinct frequency regimes due to mesoscopic FPD. These frequency regimes are separated by two characteristic frequencies. When one of the two types of layers has an infinite thickness, only one of these frequencies remains finite and thus, for $\omega < \omega_B$, there are only two frequency regimes. Our model corresponds to this limiting case. The characteristic frequency for the transition between the two regimes is (Müller and Rothert, 2006)

$$\omega_m = 2\pi f_m = \left(\frac{2}{h}\right)^2 D^f_{eff}, \tag{18}$$

where the effective fracture diffusivity D^f_{eff} is defined as

$$D^f_{eff} = \left(\frac{e_b^2}{e_f^2 + e_f e_b}\right) D^f, \tag{19}$$

with the effusivity

$$e = \frac{\kappa}{\eta\sqrt{D}}. \tag{20}$$

In Eqs. 19 and 20, the subscripts b and f refer to background and fracture parameters, respectively. From Eqs. 16 and 18, it is clear that ω_m corresponds to an effective diffusion length L_{eff} equal to half the fracture aperture. When one of the layers is much more compliant and permeable than the other, Brajanovski et al. (2006) showed that

$$\omega_m \approx \left(\frac{2N_f}{N_b h}\right)^2 D^b. \tag{21}$$

Hence, even though ω_m depends on the permeability of both layers, for the fracture model considered here $\omega_m \propto \kappa_b$ and is insensitive to the value of κ_f. This implies that the seismic reflectivity of an open fracture is rather insensitive to its permeability value.

For frequencies $\omega \ll \omega_m$, there is enough time in one half-cycle of the seismic wave for the fluid pressure to equilibrate in the whole system and the fracture is relaxed. In this case, the stiffening effect of the fracture fluid is minimal and, consequently, fracture stiffness is minimal. Conversely, when $\omega \gg \omega_m$ there is no time for communication between the fluid of the fracture and that of the background and the fracture behaves as undrained. In this condition, the stiffening effect of the fracture fluid is maximal and, therefore, fracture stiffness is maximal. In this limit of sealed interfaces, the stiffness of the poroelastic model is the same as that of the elastic model.

In the analysis of Müller and Rothert (2006) intertial effects were neglected. However, if we consider such effects, there is yet a third regime arising at very high frequencies

$\omega > \omega_B$. Here, inertial forces play an important role and, correspondingly, the low-frequency approximation for wave propagation is no longer valid. The velocity dispersion due to global flow increases the apparent stiffness of the saturated fracture with respect to the undrained situation described before. These effects are present neither in the elastic model nor in the poroelastic low-frequency approximation and, consequently, the agreement between the models is expected to decrease.

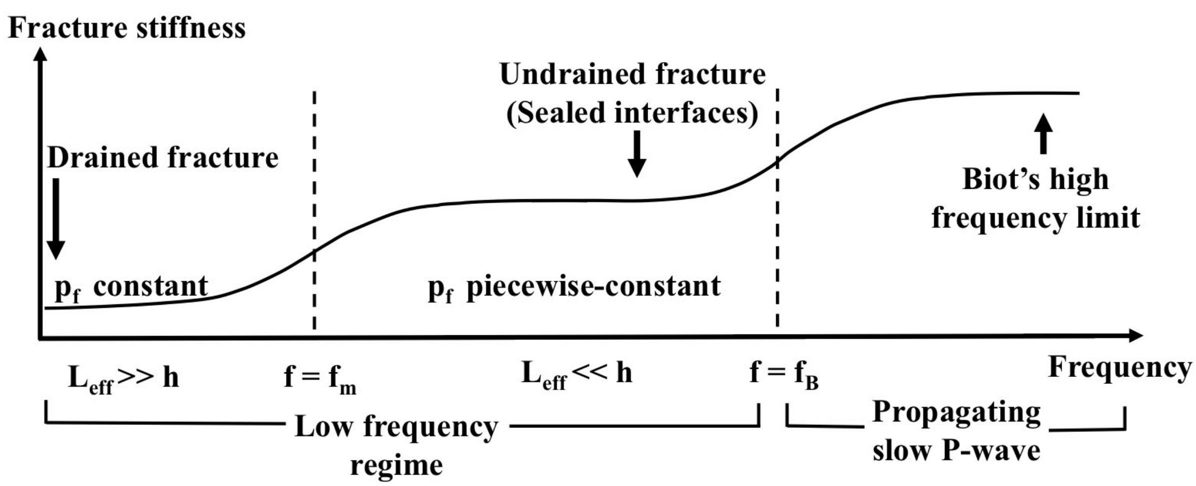

FIG. 2. (Color Online) Schematic representation of the stiffness variation of a saturated fracture as a function of frequency.

Fig. 2 shows the different frequency-regimes that the considered fracture-background system experiences in a poroelastic context. For a given ratio between wavelength and fracture aperture, the reflectivity of a fracture is mainly controlled by the stiffness contrast with respect to the background. Hence, the frequency-dependent effects produced by the saturating pore fluid in the fracture are expected to affect the reflectivity. In the following, we analyse quantitatively to what extent these fluid effects manifest themselves in the reflectivity of an individual fracture.

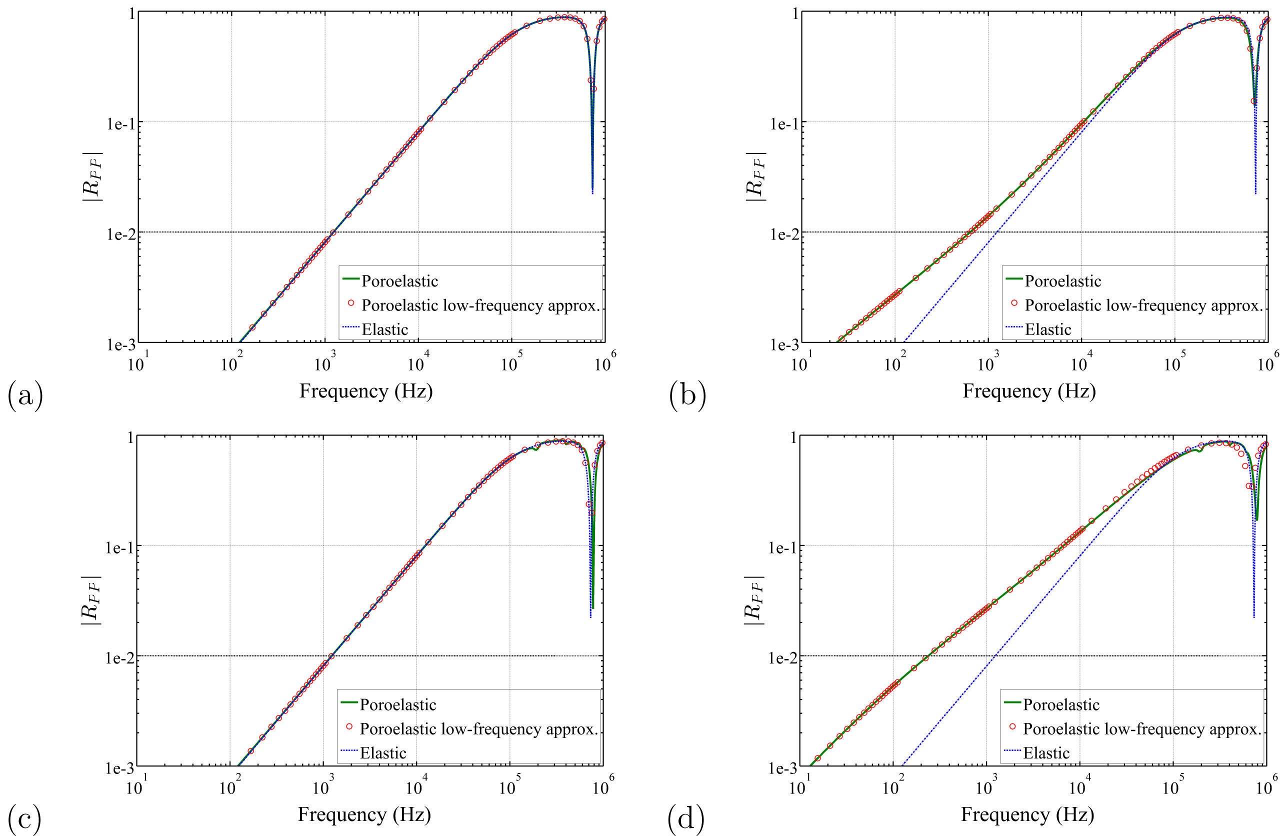

FIG. 3. (Color Online) Elastic as well as full and low-frequency poroelastic models. a) Regime with no mesoscopic and no global flow, b) regime with no global flow, c) regime with no mesoscopic flow, and d) reference scenario. The dashed lines correspond to $|R_{PP}|$ =0.01, which is considered as the threshold value for seismic detectability.

III. FREQUENCY-DEPENDENT FLUID-RELATED EFFECTS

For the following analysis, we assume that the fracture is embedded in an homogeneous background, that is, Ω_1 and Ω_3 are identical. Unless indicated otherwise, the material properties are those given in Table 1. The background properties correspond to those of a sandstone and were chosen following Nakagawa and Schoenberg (2007). We characterize the fracture dry frame properties in terms of the dry normal compliance

$$\eta_N = \frac{h}{K_{\mathrm{m}}^{\mathrm{f}} + \frac{4}{3}\mu_{\mathrm{m}}^{\mathrm{f}}} = \frac{h}{H_D^{\mathrm{f}}}, \tag{22}$$

and the shear compliance

$$\eta_T = \frac{h}{\mu_{\mathrm{m}}^{\mathrm{f}}}, \tag{23}$$

where the superscript f refers to fracture parameters and H_D is the dry P-wave modulus. According to Nakagawa and Schoenberg (2007), we choose for the fracture compliance $\eta_T = 3\times10^{-11}$ m/Pa and $\eta_N = 10^{-11}$ m/Pa and thus obtain $\mu_{\mathrm{m}}^{\mathrm{f}} = 0.033$ GPa and $K_{\mathrm{m}}^{\mathrm{f}} = 0.056$ GPa for the considered fracture aperture of 1 mm. Both the fracture and the background are saturated with brine (Table 1).

We consider four scenarios with varying permeabilities of the fracture and background to distinguish the different frequency regimes of fluid flow effects and to quantify the corresponding impacts on seismic reflectivity. For comparison, we include the responses obtained using the full poroelastic model, its low-frequency approximation, as well as the elastic model. In order to separate the different fluid flow effects, we consider for some of the scenarios unrealistically low values of the fracture permeability and the background tortuosity. It is important to mention that even though, for brevity, we show the comparisons only for normal incidence for the first three cases, the observations and conclusions obtained in this section also hold for oblique incidence angles.

A. Undrained fracture in viscous forces dominated regime

First, we consider the case in which the reflection coefficients from the three models are expected to agree. This scenario corresponds to the case of low frequencies in relation with Biot's global flow and high frequencies in terms of mesoscopic FPD, that is, $\omega_m < \omega < \omega_B$. To have such situation, we consider very low permeabilities for the background and the fracture ($\kappa^b = 1 \times 10^{-6} D$, $\kappa^f = 0.01 D$), which in turn implies a very low value for the characteristic frequency related to mesoscopic FPD ($f_m = 6.71 \times 10^{-4}$Hz). Correspondingly, the fracture behaves as being sealed for the considered frequencies. Moreover, the Biot's characteristic frequencies are $f_{Biot}^f = 1.29 \times 10^7$ Hz and $f_{Biot}^b = 8.06 \times 10^9$ Hz for the fracture and background material, respectively. These characteristic frequencies are located well above the considered frequency range and, thus, velocity dispersion effects due to global flow are negligible.

Figure 3a shows that there is indeed excellent agreement between the reflection coefficients obtained from the three models. We observe that at a frequency of $\sim 7.7 \times 10^5$ Hz, the first resonance of the fast P-wave within the fracture occurs, as at this frequency $\lambda_{P_1} = 2h$, with λ_{P_1} denoting the fast P-wavelength in the fracture. Due to the very low permeability values chosen for the analysis, we observe that even at this resonance frequency the reflection coefficients agree very well among the three models.

B. FPD between the fracture and background

In order to isolate the impact on seismic reflectivity due to FPD, we consider a scenario corresponding to the case of low frequencies with respect to Biot's global flow for which FPD effects are expected to arise. To this end, we assume values of $\kappa^b = \kappa^f = 0.01D$ for the background and fracture permeability, and a tortuosity $S = 1$ for both media. Biot's characteristic frequencies, therefore, are $f^f_{Biot} = 1.3 \times 10^7$ Hz and $f^b_{Biot} = 2.4 \times 10^6$ Hz, whereas f_m is 6.7 Hz. In this case, as f_m is larger than in the previous case, changes of the stiffness of the saturated fracture due to FPD are expected to be more important. Fig. 3b shows that, indeed, there are significant discrepancies between the elastic and the two poroelastic models for frequencies below about 3×10^4 Hz. For such frequencies, FPD between fracture and background is significant, thus reducing significantly the stiffness of the saturated fracture. The resulting increase of stiffness contrast between the fracture and the background explains the fact that for such frequencies the reflection coefficient is higher when FPD effects are taken into account. As the frequency increases, there is less time for fluid pressure exchange between fracture and background and, thus, the discrepancies between the elastic and poroelastic responses decrease. It is important to notice that, contrary to *Case A*, at frequencies close to the resonance frequency, the differences become important again. As Biot global flow effects are negligible for the considered frequency range, which is suggested by the very good agreement between the poroelastic response and the corresponding low-frequency approximation, the observed discrepancies between the elastic and poroelastic models are still given by FPD.

C. Global fluid flow inside the fracture

To analyze the impact of global flow inside the fracture on the reflectivity, we consider the case of a fracture having its characteristic Biot's frequency lying inside the considered frequency range, but for which the mesoscopic characteristic frequency and Biot's characteristic frequency for the background lie outside this range. To this end, we consider again a very low permeability for the background ($\kappa^b = 1 \times 10^{-6} D$) but, in this case, we increase the fracture permeability ($\kappa^f = 100D$), which results in the following characteristic frequencies: $f^f_{Biot} = 1290$ Hz and $f^b_{Biot} = 8.06 \times 10^9$ Hz, and f_m is $6.71{\times}10^{-4}$ Hz.

As FPD effects have been minimized, all models agree very well on the low-frequency side of the spectrum (Fig. 3c). At higher frequencies, in addition to the differing resonance frequencies, there are some small reverberations in the fast P-wave reflectivity, which are directly related to the resonance of the slow P-wave in the fracture. The latter behaves as a propagating wave inside the fracture, because these frequencies are much higher than f^f_{Biot}. This behavior can be reproduced neither by the poroelastic low-frequency approximation nor by the elastic model. The first resonance of the slow P-wave occurs for $\lambda_{P_2} = 2h$.

Even though not shown for brevity, we also analyzed the case in which only Biot's characteristic frequency of the background lies in the range of frequencies considered. The results indicate that the discrepancies among the models present the same overall behaviour. We can therefore conclude from this analysis that global flow effects on the reflectivity of a single fracture are rather negligible, especially for the frequencies typically considered in seismic experiments. We have verified that this result also holds for S-wave reflectivity.

D. Mesoscopic and global flow effects

Lastly, Fig. 3d) shows a more realistic scenario corresponding to the properties in Table 1. In this case, Biot's characteristic frequencies are $f^f_{Biot} = 1290$ Hz and $f^b_{Biot} = 8.06 \times 10^4$ Hz, whereas the mesoscopic characteristic frequency is $f_m = 67.1$ Hz. In this case, both FPD and global flow effects described for the previous three scenarios are at play in the considered frequency range.

For frequencies below about 3×10^4 Hz, the elastic model systematically underestimate the reflection coefficient computed from the poroelastic models. This is due to significant FPD occurring between the fracture and the background, which reduces the apparent stiffness of the saturated fracture, thus increasing its mechanical contrast with respect to the background. These FPD effects can be quite strong and produce significant discrepancies between the elastic and poroelastic responses. For instance, at 6.7 kHz, the fast P-wave reflection coefficient predicted by the poroelastic model is 0.1 whereas for the elastic model it is approximately 0.05.

For frequencies above $3{\times}10^4$ Hz, there is not enough time for FPD and, consequently, there is good agreement between the elastic and poroelastic responses. However, there are significant discrepancies for frequencies close to the resonance frequencies as, in addition to the remaining FPD effects, velocity dispersion effects due to global flow arise. We can also see that there is very good agreement between the poroelastic models, except for frequencies larger than the Biot's characteristic frequencies, which is due to the fact that the low-frequency approximation is not valid anymore.

In addition to the frequency dependence of the discrepancies between the elastic and poroelastic models, it is interesting to study, for this more realistic scenario, the corresponding dependence on incidence angle as well as the case of S-wave reflectivity. As the discrepancies between elastic and poroelastic models are mainly due to FPD effects, we restrict the analysis to frequencies between 50 and 10^4 Hz, thus covering the seismic and sonic frequency ranges.

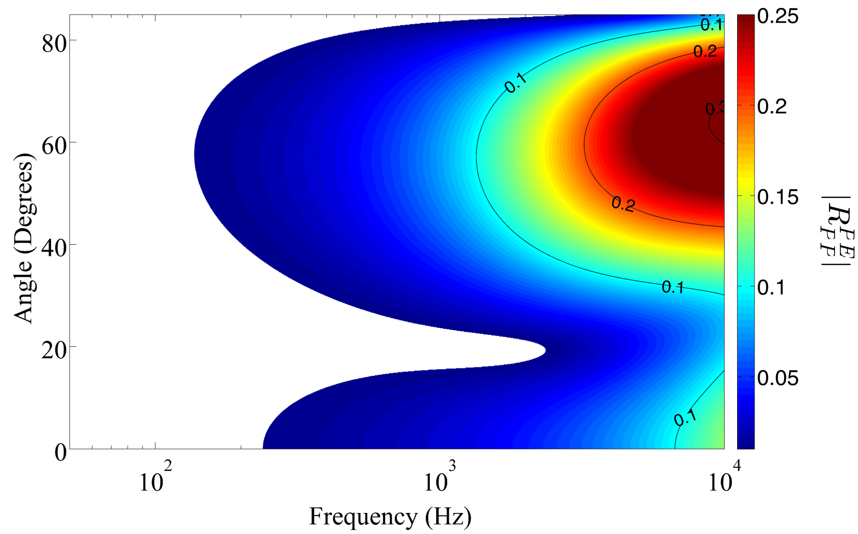

a)

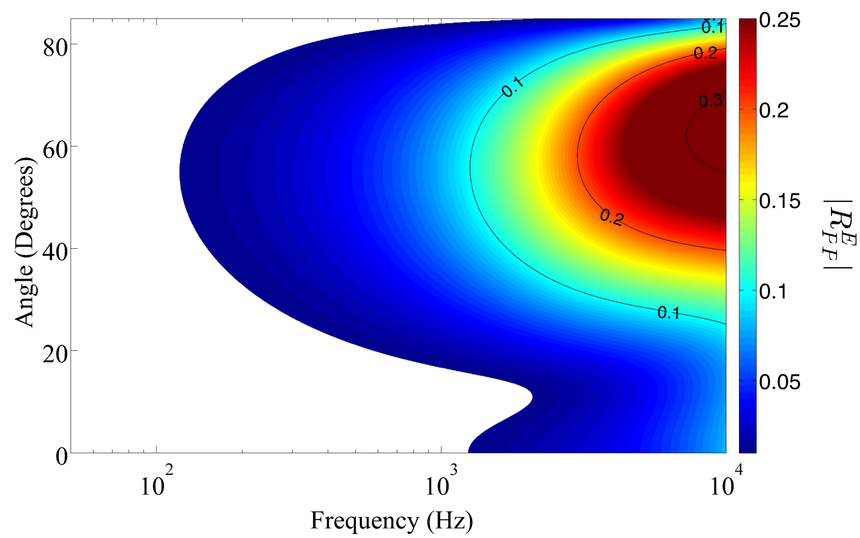

b)

FIG. 4. (Color Online) Absolute value of fast P-wave reflection coefficient for a) a poroelastic and b) an elastic fracture model as a function of incidence angle and frequency. The considered material properties are given in Table 1.

Fig. 4 shows the magnitude of the elastic and poroelastic P-wave reflection coefficient as a function of frequency and incidence angle. The white zones in Fig. 4 correspond to the regions where the reflection coefficients are lower than 0.01, which is the threshold value of minimum reflectivity adopted for this work. A distinct feature in the P-wave reflectivity is the presence of a "tongue" of this blind zone, which implies that for a given range of incidence angles the reflection coefficient of the fracture is minimal. A more detailed analysis shows that this phenomenon is due to a change of polarity of the reflection coefficients. By comparing Figs. 4a and b, we note that the range of angles of this minimum differs for the poroelastic and elastic models, thus indicating that the differences between the models are dependent on the incidence angle. While for incidence angles below $\sim 20°$, where the reflectivity for the poroelastic model is at its minimum, the elastic model underestimates the reflection coefficients, the opposite is the case for larger incidence angles. Similarly, we show in Figs. 5a and b the S-wave reflection coefficient for the elastic and poroelastic models as a function of frequency and incidence angle. As expected, S-wave reflectivity is zero for the normally incident fast P-wave. In addition, the patterns of reflectivity for S-waves are similar for both models. However, for any angle of incidence the coefficients are always slightly larger for the poroelastic model.

To quantify FPD effects on the reflection coefficient, we compute the relative differences $\delta R_{PP} = \frac{R^{PE}_{P_1P_1} - R^{E}_{PP}}{R^{PE}_{P_1P_1}}$ and $\delta R_{PS} = \frac{R^{PE}_{P_1S} - R^{E}_{PS}}{R^{PE}_{P_1S}}$, where the superscripts PE and E refer to the full poroelastic and elastic models, respectively. Figures 6a and 6b show the corresponding relative differences for the cases shown in Figs. 4 and 5. The blind zone in the map was chosen based on the poroelastic model. For the P-wave reflectivity, we observe significant discrepancies between the two models and, thus, FPD effects, particularly for relatively low frequencies and low incidence angles, where the elastic model substantially underestimates the reflectivity of the fracture (Fig. 3). The angle dependence of the discrepancies is expected, as for quasi-horizontal directions of wave propagation the incident P-wave does not manage to effectively compress the fracture and, thus, FPD effects on the stiffness of the saturated fracture and, thus, on reflectivity, get less significant.

For the S-wave reflectivity, the discrepancies are considerably smaller compared to those for P-waves, which implies that this wave mode is less affected by changes in fluid pressure than the P-wave. This may in part be due to the fact that for close to normal direction of propagation of the incident fast P-wave, for which a significant fluid pressure change inside

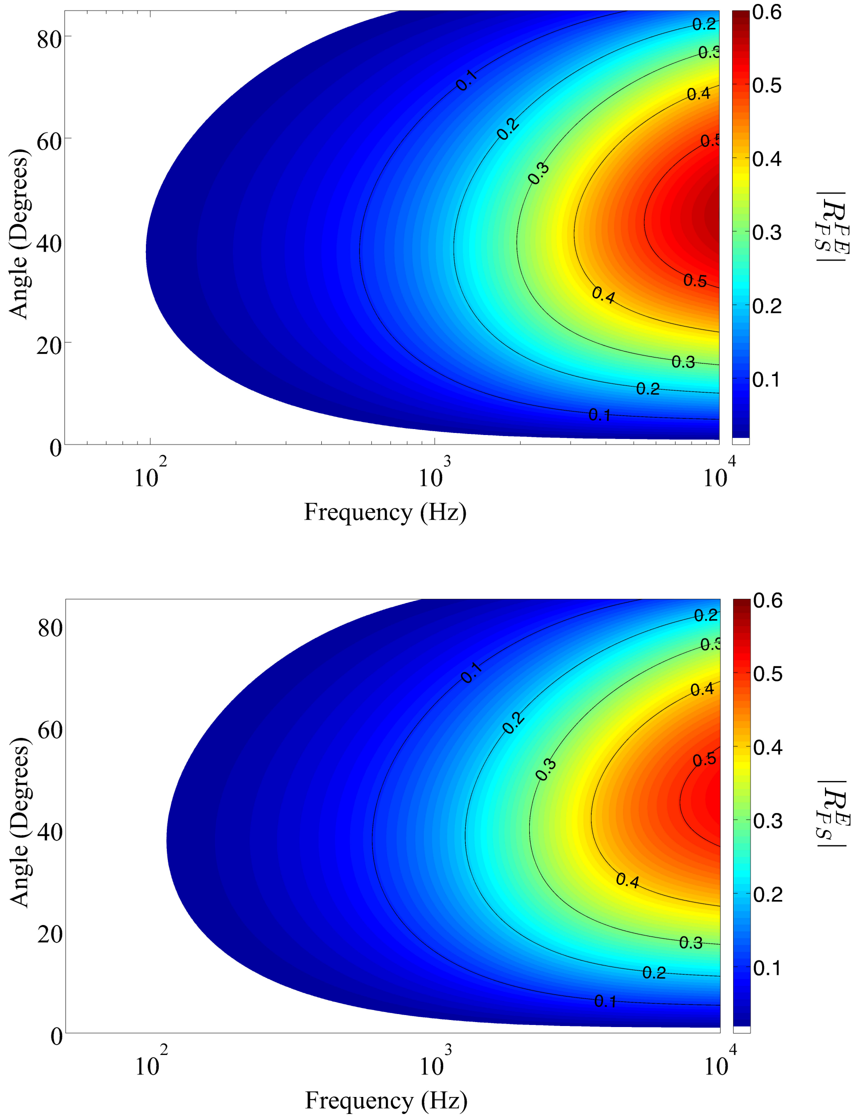

a)

b)

FIG. 5. (Color Online) Absolute value of S-wave reflection coefficient for a) a poroelastic and b) an elastic fracture model as a function of incidence angle and frequency. The considered material properties are given in Table 1.

the fracture may arise, S-wave reflectivity is minimal.

The FPD processes occurring between the fracture and the embedding background can also be interpreted as energy conversions from the incident fast P-wave into slow P waves at the fracture interfaces. To illustrate this, we show in Fig. 7 the energy conversion to reflected

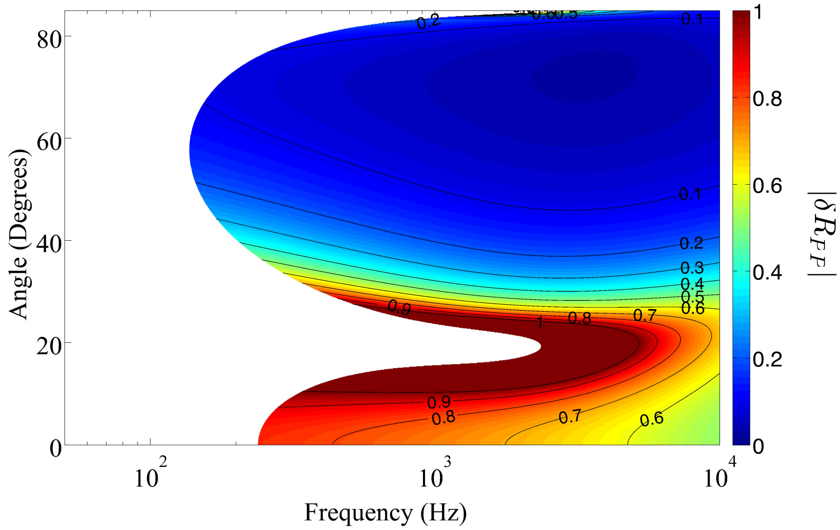

a)

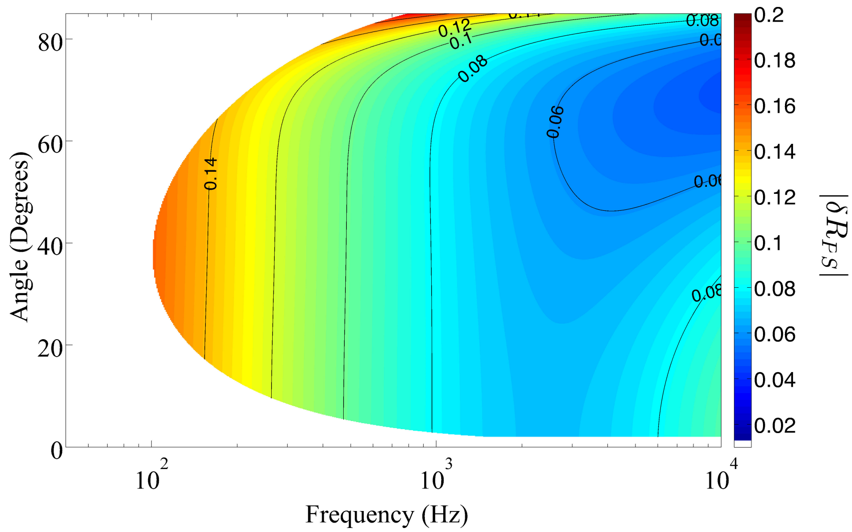

b)

FIG. 6. (Color Online) Magnitude of relative differences between the elastic and poroelastic models for a) fast P-wave and b) S-wave reflection coefficients. The considered material properties are given in Table 1.

and transmitted slow P-waves relative to that of the fast P-wave reflection (Appendix C). That is, the amount of incident energy flux that is converted at the fracture interfaces from the incident fast P-wave to reflected and transmitted diffusive waves in the background divided by the energy converted to the reflected fast P-waves. The clear correlation between

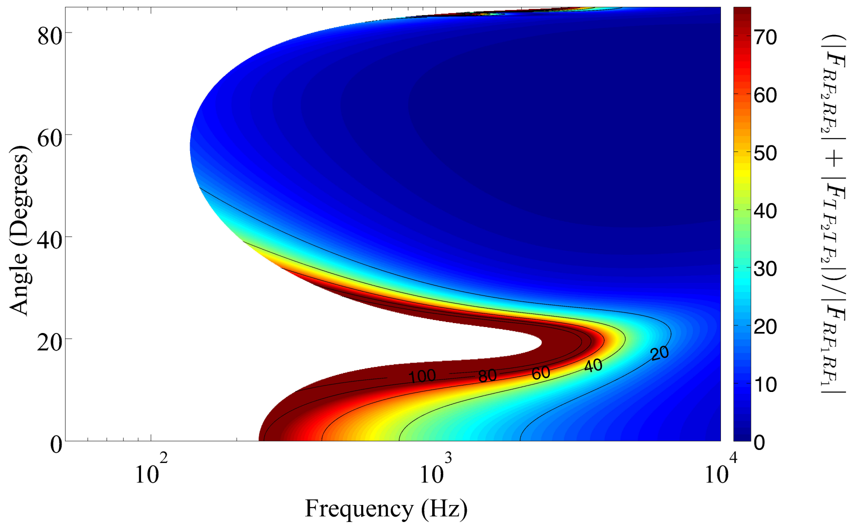

FIG. 7. (Color Online) Slow P-wave reflected and transmitted orthodox fluxes relative to the reflected orthodox flux of the fast P-wave. The considered material properties are given in Table 1.

Figs. 7 and 6a illustrates the fact that in the low-frequency regime, the relative differences between the reflectivity for pure elastic and poroelastic fracture models are governed by the FPD produced at the boundaries of the fracture and thus represent a measure of how this process affects the reflectivity.

IV. SENSITIVITY ANALYSIS OF FPD EFFECTS

The analysis performed in the previous section indicates that while global flow effects on the reflectivity of a fracture are rather negligible, especially in the frequency range usually considered for practical applications, FPD effects can be quite strong and produce significant discrepancies between the elastic and poroelastic responses. In this section, we perform a sensitivity analysis in order to determine which parameters control this physical process and to explore in which cases these effects are expected to have a significant impact on the fracture reflectivity.

The physical properties previously used for *Case D* (section III) are considered as a reference scenario. Based on this case, we explore how the discrepancies between the elastic and poroelastic models change as we modify different material and geometrical properties of the fracture-background system. In particular, we consider different permeabilities and stiffnesses of the background as well as different apertures, dry-frame properties, and pore fluids of the fracture. We do not include in this study the analysis of the sensitivity of the discrepancies to changes in fracture permeability. Since in the case of open fractures, as the ones studied in this work, the seismic reflectivity is rather insensitive to fracture permeability. In addition, only the results for the relative differences in P-wave reflectivity are discussed as the relative differences for the S-wave reflection coefficients turned out to be rather negligible.

A. Saturating pore fluid in fracture

Fig. 8 shows the poroelastic reflection coefficients and the relative difference δR_{PP} for a fracture saturated with gas ($K_f = 0.05543$ GPa, $\rho_f = 139.8$ kg/m^3, $\eta_f = 0.00022$ Poise). The saturating pore fluid of the background is water. The mechanical compliance of the fracture strongly depends on the saturating pore fluid. It increases for more compressible fluids, which increases the reflectivity of the fracture, as can be verified by comparing Figs. 4a and 8a. This, in turn, implies that the blind zone gets smaller with increasing fluid compressibility for close to normal direction of propagation while its "tongue" shifts towards higher incidence angles. Even though the reflectivity increases with the compressibility of the pore fluid in the fracture, the discrepancies between the poroelastic and elastic responses are reduced (Figs. 6a and 8b). Because of the high compressibility of the gas, the excess pore pressure induced within the fracture is smaller compared to that for a less compressible fluid and, thus, the fluid pressure gradient between fracture and background is reduced. Consequently, FPD between these two regions and its effects on the reflectivity, become less significant.

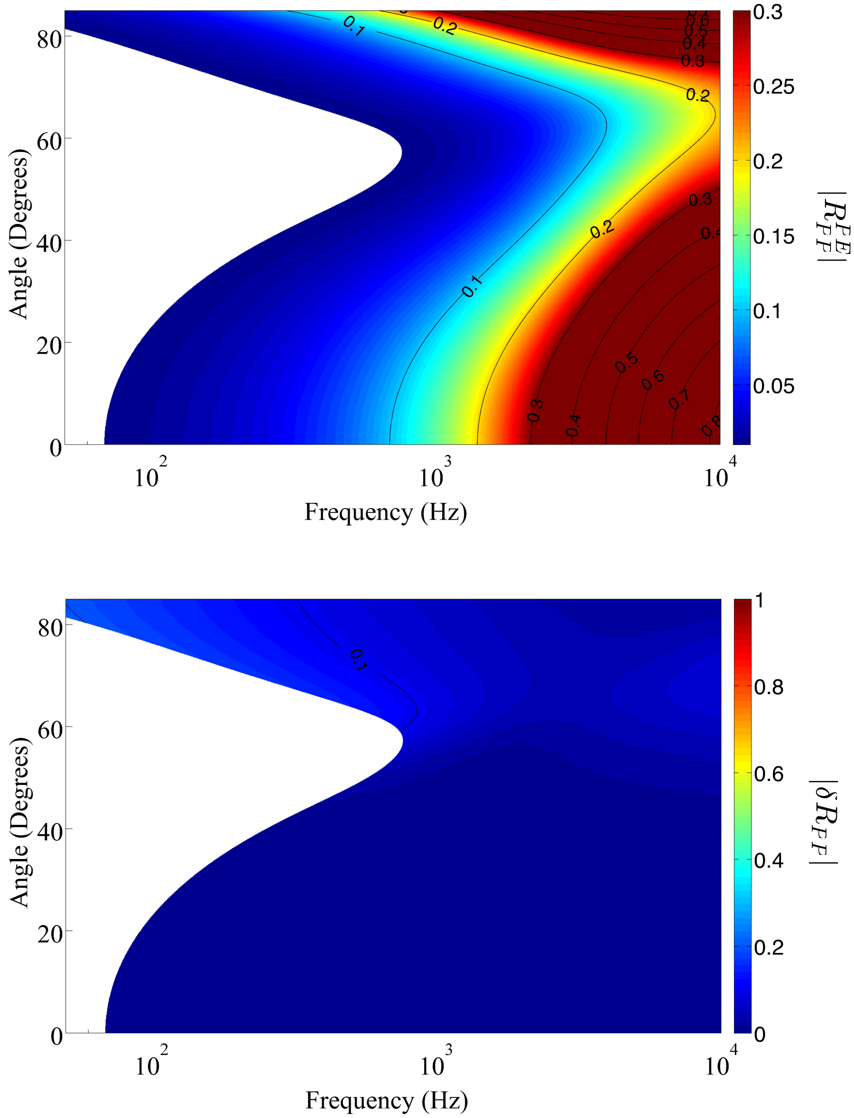

a)

b)

FIG. 8. (Color Online) Absolute value of a) P-wave reflection coefficient of a gas-saturated poroelastic fracture as a function of incidence angle and frequency and b) magnitude of the relative differences between the elastic and poroelastic models.

B. Background permeability

As shown in the previous section, FPD between the fracture and the background is strongly influenced by the permeability of the latter. To further explore the corresponding effects on the reflectivity of a fracture, we show in Fig. 9 the relative difference δR_{PP} for

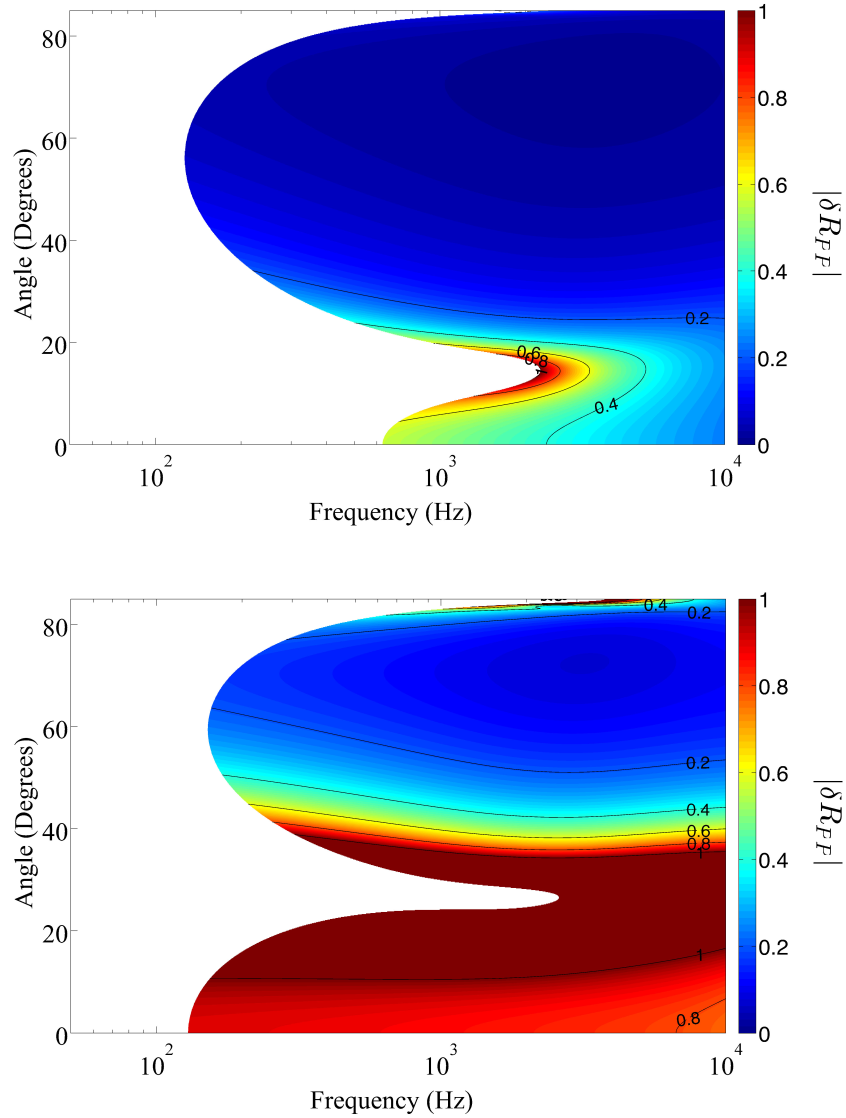

a)

b)

FIG. 9. (Color Online) Absolute value of the relative difference of P-wave reflection coefficients obtained from elastic and poroelastic models as a function of incidence angle and frequency for background permeabilities of a) $\kappa = 0.01D$ and b) $\kappa = 1D$.

a more and a less permeable background compared to the reference scenario. We observe increasing discrepancies between the models for all incidence angles as the permeability of the background increases. This is due to the fact that, for very low permeabilities, significant FPD takes place only for very low frequencies, for which the fluid has enough time during an oscillatory half-cycle to flow into the background or out of it. This can also be seen by taking into account that, for a fracture that is much more permeable than the embedding background, we have, $\omega_m \propto \kappa_b$, as discussed before. For such low frequencies, the reflection coefficient is negligible and, thus, the corresponding FPD effects on the reflectivity cannot be observed. Conversely, for higher background permeabilities, these FPD effects occur at higher frequencies, for which the reflection coefficients assume significant values, and hence the discrepancies between the two models become important.

For larger permeabilities, the "tongue" of the blind zone also shifts towards larger incidence angles and becomes narrower. Moreover, the comparison of the blind regions indicates that for such permeabilities, the reflection coefficients are larger at low incidence angles.

We show in Fig. 10 that the change of FPD effects due to the background permeability, can be illustrated by the amount of incident energy flux that is converted at the fracture interfaces into reflected and transmitted diffusive waves in the background, for fixed frequencies of 100 Hz and 10 Hz. We observe that the energy conversion to diffusive slow P-waves across a fracture follows an attenuation-type curve, as in the low-frequency regime ($f < f_{Biot}$) this is a measure of attenuation (Müller et al., 2010). In both cases, the slow P-wave energy conversion has a peak for a background permeability for which $f = f_m$ (see vertical lines in Fig. 10). By comparing the plots for both frequencies, it is clear that the maximal FPD effects shift towards lower frequencies for less permeable backgrounds. Lastly, from the definition of the energy flux converted to slow P-waves (Appendix C), minimum energy conversion to diffusive waves, for a given frequency, occurs for (i) background permeabilities such that the frequency considered is higher than f_m, that is, in the high-frequency regime, where the fluid pressure in the fracture is maximum but the relative fluid displacement tends to be negligible; and (ii) in the cases for which the fixed frequency is low in relation to f_m, producing maximum wave-induced fluid flow with approximately the same fluid pressure in the fracture and the background.

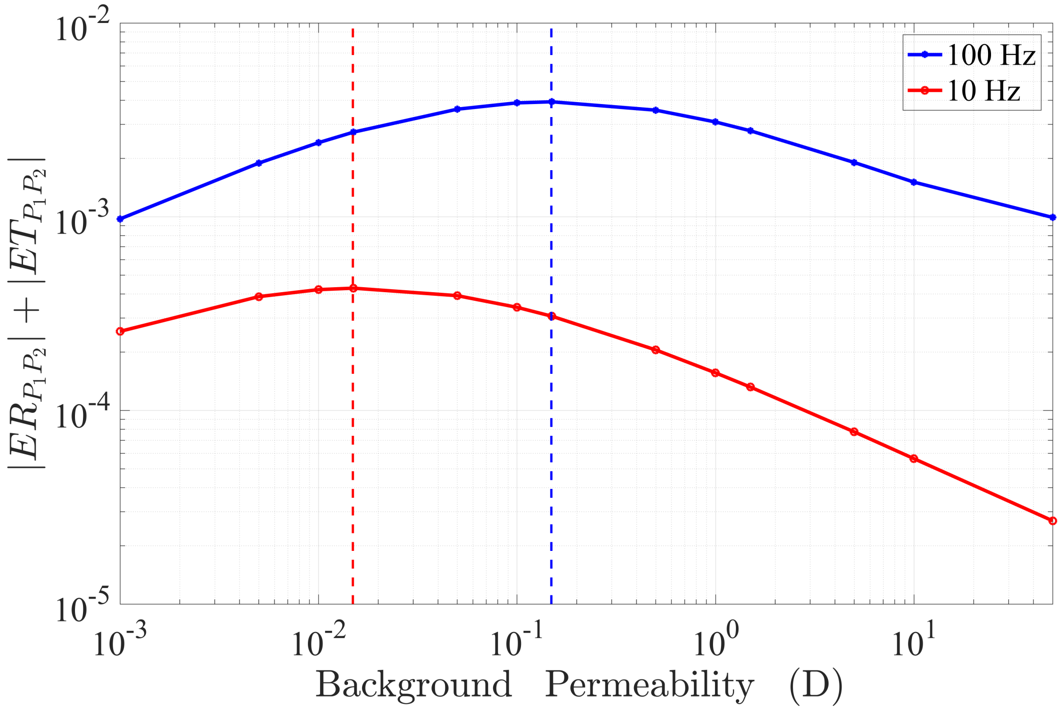

FIG. 10. (Color Online) Sum of slow P-waves energy reflection and transmission coefficients for poroelastic model as a function of background permeability, for frequencies of 100 Hz and 10 Hz. The red and blue vertical lines correspond to the background permeabilities for which the mesoscopic characteristic frequencies of the model are equal to 10 Hz and 100 Hz, respectively.

C. Fracture and background dry-frame stiffness

In order to analyze the role played by the mechanical properties of the fracture dry-frame, we show in Fig. 11 the relative difference δR_{PP} for a stiffer and for a softer fracture compared to the reference scenario. As expected, the seismic reflection is strongly affected by the stiffness of the fracture. The blind zone gets significantly larger in the case of a stiffer fracture. This is expected, as the compressibility contrast with respect to the background is reduced and, consequently, the reflection coefficients get smaller. The "tongue" of minimum reflectivity appears at larger incidence angles for stiffer fractures. The mesoscopic

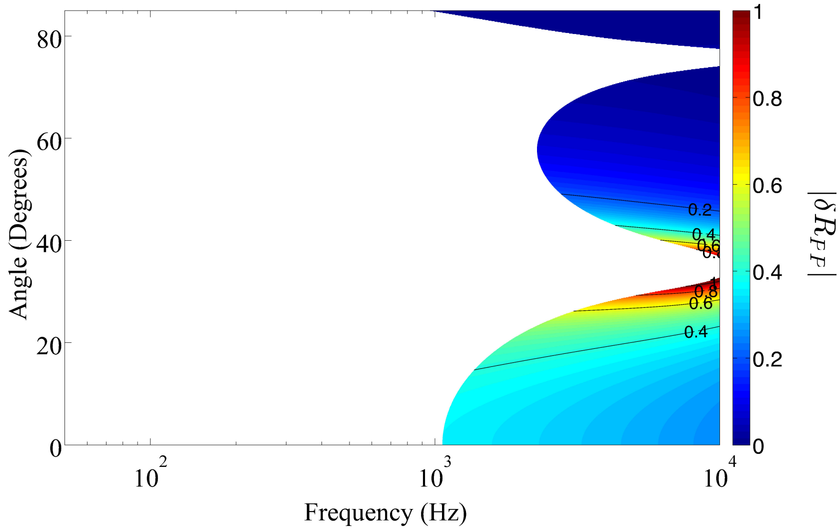

a)

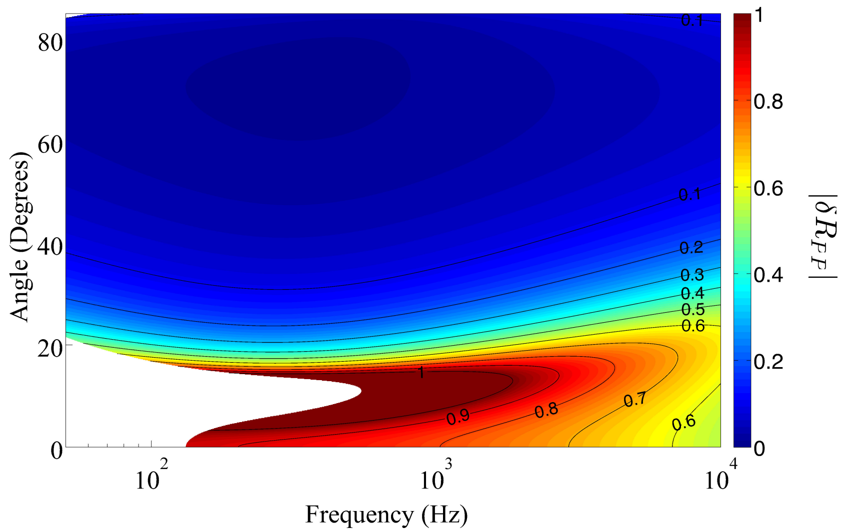

b)

FIG. 11. (Color Online) Absolute value of the relative difference of P-wave reflection coefficients for elastic and poroelastic models as a function of incidence angle and frequency for a) a fracture stiffer (K_m=0.55 GPa and μ_m=0.33 GPa) and b) softer (K_m=0.0056 GPa and μ_m=0.0033 GPa) than the reference scenario.

characteristic frequencies are 4049 Hz and 0.7 Hz for the scenarios depicted in Figs. 11a and 11b, respectively. Despite the fact that for the stiffer fracture the considered frequency range includes the characteristic mesoscopic frequency, whereas this is not the case for the softer fracture, the agreement between the two models improves for the stiffer fracture. This implies that, while the position of the maximal FPD effects is determined by the mesoscopic characteristic frequency, the magnitude of the FPD effects on the reflectivity is controlled by the compressibility contrast. This is due to the fact that stiffer fractures produce less FPD and, thus, cause smaller departures of the stiffness of the fracture with respect to the elastic undrained limit. This results in a better agreement with respect to the elastic model in comparison with softer fractures.

The analysis of FPD effects on the seismic reflectivity for the case of varying background dry-frame stiffness is not shown as it exhibits the same behavior described above. That is, even though considering a softer, yet still stiffer than the fracture, background compared to that of the reference scenario, results in a shift of FPD effects towards the frequency range considered in the analysis, both the reflection coefficients and the intensity of the FPD effects get smaller. This again is due to a reduction of the stiffness contrast with respect to the fracture.

D. Fracture aperture

Fig. 12 shows the relative difference δR_{PP} for two different fracture apertures. The physical properties of the fracture remain unchanged and are those given in Table 1. We observe that as the fracture aperture increases, the reflectivity increases for all incidence angles. The latter is evidenced by a reduction of the blind zone in the case of a thicker fracture and is due to the fact that the ratio between the aperture and the wavelength of the incident wave becomes larger. Moreover, the "tongue" of the blind zone shifts towards smaller incidence angles for thicker fractures.

In Fig. 12a, that is for a 10-mm-thick fracture, we observe a local maximum in $|\delta R_{PP}|$ at approximately 8 kHz. This frequency coincides with the first resonance within the fracture for the elastic model at oblique incidence, whereas for the poroelastic model the lowest frequency resonance is $\sim$10 kHz.

In addition, Fig. 12 shows that the differences between the poroelastic and elastic models become smaller for thicker fractures. To further explore this observation, we first remove

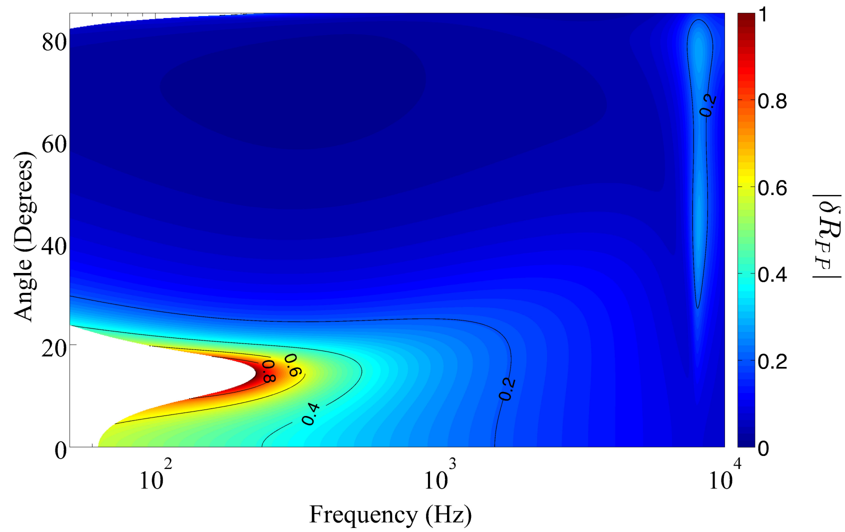

a)

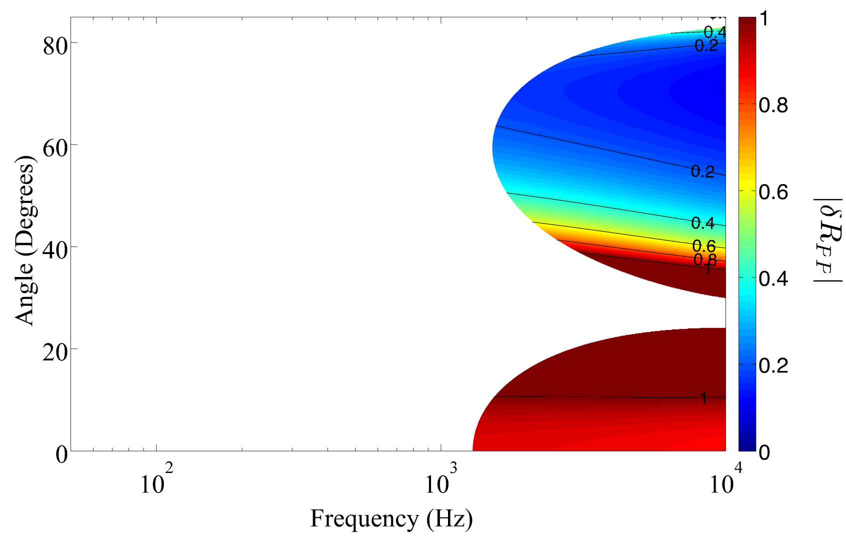

b)

FIG. 12. (Color Online) Absolute value of the relative difference of P-wave reflection coefficients for elastic and poroelastic models as a function of incidence angle and frequency for fracture apertures of a) 10 mm and b) 0.1 mm.

the changes in reflectivity due to changes in the ratio wavelength to fracture aperture. That is, we consider a constant ratio between the two quantities for three cases. In Fig. 13a we show P-wave reflectivity for the elastic model as a function of incidence angle. The fracture thickness considered in cases 1, 2, and 3 are 1, 10, and 0.1 mm respectively. The frequencies chosen for these three cases are $f = 1, 0.1$, and 10 kHz, respectively, which implies that the ratio between the incident wavelength and the fracture aperture remains constant at λ / $h \sim$ 3.2×10^3. As a consequence, the three curves are exactly the same, thus illustrating that for the elastic case the reflectivity of the fracture depends exclusively on this geometrical relation (Li et al., 2014). Fig. 13b shows the corresponding P-wave reflectivity of the poroelastic model. Even though the ratios between wavelength and fracture aperture are the same in the three cases, the reflectivities are quite different, which illustrates that the FPD effects differ for the three cases considered. Indeed, the mesoscopic characteristic frequencies f_m for the three cases are 67.13, 0.6713, and 6713 Hz, respectively. Compared to the elastic reflectivity, case 3 shows the largest differences, which is due to more pronounced FPD effects as indicated by f_3/f_m=1.49. Conversely, case 2 shows a response quite close to that of the elastic limit, since in this case the considered frequency is significantly higher than the corresponding mesoscopic frequency (f_2/f_m=149). This analysis therefore indicates that, due to FPD effects, the same ratio between incident wavelength and the fracture thickness does not yield the same reflectivity.

This can be shown by considering a case 4 with the same frequency and model parameters as in case 3 but with a less permeable background (κ_b = 0.01 D instead of κ_b = 0.1 D), which implies that the mesoscopic characteristic frequency f_m is 671.3 Hz, and, thus we have f_4/f_m=14.9 as in case 1 (Fig. 13b). Hence, the reflectivity for cases 1 and 4 is the same because we are considering the same values for λ/h and f/f_m. Thus, the thickness of the fracture has the same effect on the relative differences as varying background permeabilities.

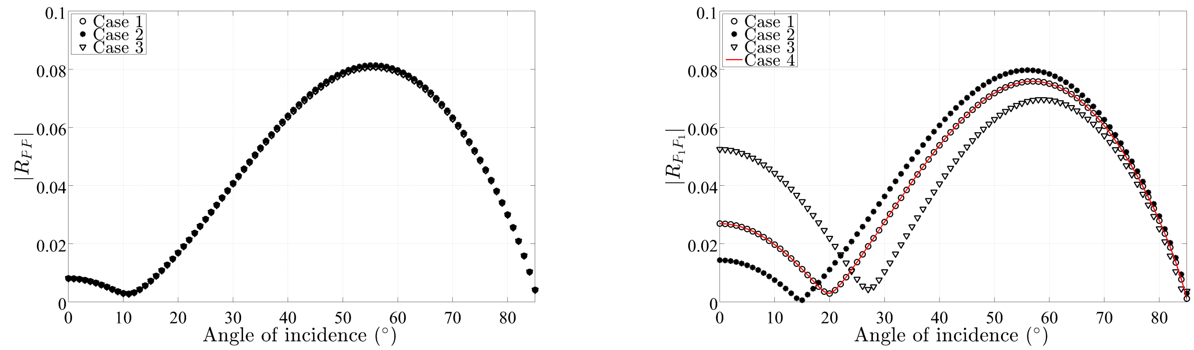

a) b)

FIG. 13. (Color Online) P-wave reflection coefficient as a function of incidence angle for equal ratios of wavelength to fracture thickness for three cases characterized by different fracture apertures (case 1: 1mm, case 2: 10mm, case 3: 0.1 mm). a) Elastic models, b) poroelastic models. Cases 3 and 4 have the same fracture thickness but a different background permeability.

V. CONCLUSIONS

In this work, we have performed a numerical analysis of FPD effects on the seismic reflectivity of a single fracture based on Biot's theory of poroelasticity. The fracture is represented as a highly compliant and porous thin layer embedded in a much stiffer and much less porous background, impinged by a plane P-wave at an arbitrary angle of incidence. In order to separate different FPD effects, we compare the resulting reflectivity curves with those obtained using a low-frequency approximation of Biot's theory as well as an elastic model with parameters defined using Gassmann's equations. Our results indicate that for realistic rock physical properties the impact of global flow on the seismic reflectivity of a fracture is rather negligible, particularly for frequencies below the resonance frequency and Biot's characteristic frequency. Conversely, FPD effects can be significant, especially for P-wave reflectivity and low incidence angles.

An exhaustive sensitivity analysis comprising a broad range of rock physical properties and seismic frequencies allows us to verify that FPD effects get particularly strong in the presence of very thin and soft fractures saturated with a liquid and embedded in a relatively high-permeability background. We also show that the dependence of FPD effects on the hydraulic, elastic, and geometrical parameters of the media implies that, in order to get the same reflectivity, it is not sufficient to consider the same ratio between seismic wavelength and fracture thickness as in a purely elastic context. Due to FPD effects, the same ratio between the frequency of the wave field and the mesoscopic characteristic frequency is also required.

In all cases considered in this analysis, there is a "tongue-shaped" zone in the incidence angle-frequency plane of the P-wave reflectivity where the fracture is seismically not visible. This zone is systematically located at lower incidence angles for the elastic model compared with its poroelastic counterpart. For incidence angles lower than the threshold value defining this "tongue" in the poroelastic model, the reflection coefficients are substantially underestimated by the elastic approach, as the latter does not include the reduction of the stiffening effect of the fluid saturating the fracture, caused by FPD. This is an important result as it implies that, for close-to-normal incidence angles, individual fractures are seismically more visible than expected based on classical elastic modelling.

Acknowledgments

This work was supported by a grant from the Swiss National Science Foundation and was completed within SCCER-SOE with the support of CTI. We wish to thank an anonymous reviewer for the comments and suggestions that helped to improve the quality of this manuscript. J.G. Rubino greatly acknowledges the financial support of the Foundation Herbette for an extended visit to the University of Lausanne.

APPENDIX A: BIOT'S COMPLEX WAVENUMBERS

The frequency-dependent viscous and mass coupling coefficients involved in the dynamic equations of an isotropic, homogeneous fluid-saturated porous medium are given by

$$\begin{aligned} b(\omega) &= \Re(\frac{\eta}{\kappa_d(\omega)}), \\ g(\omega) &= \frac{1}{\omega}\Im(\frac{\eta}{\kappa_d(\omega)}). \end{aligned} \tag{A1}$$

where $\kappa_d(\omega)$ is the dynamic permeability, which characterizes the transition between the frequency regime where the relative fluid displacement is governed by the viscous forces and that where the inertial forces predominate. For the Fourier transform sign convention adopted in this work, this dynamic permeability can be expressed as (Johnson et al., 1987)

$$\kappa_d(\omega) = \kappa\left(\sqrt{1+\frac{4i\omega}{n_j\omega_B}}+\frac{i\omega}{\omega_B}\right)^{-1}. \tag{A2}$$

In Eq. A2, n_j is a parameter related to the permeability, the formation resistivity factor, and the pore geometry of the rock. We use a value of 8 which is a common choice for sandstones (Nakagawa and Schoenberg, 2007).

As we assume plane-wave propagation, regardless of the wave mode of propagation, the response in the material has the form

$$\begin{aligned} \mathbf{u} &= Ae^{i(\omega t-\mathbf{k}.\mathbf{x})}\breve{u}, \\ \mathbf{w} &= Be^{i(\omega t-\mathbf{k}.\mathbf{x})}\breve{w}. \end{aligned} \tag{A3}$$

Here, $\breve{u}$ and $\breve{w}$ are the unit vectors defining the polarization of the response, and $\mathbf{x}$ denotes the particle position vector, where, in this context, we define a particle as an elementary volume of the fluid-saturated porous medium. Moreover, $\mathbf{k}$ is the wave vector, which can be written as

$$\mathbf{k} = k(\omega)\breve{k}, \tag{A4}$$

where $k(\omega)$ is the complex-valued wavenumber, and $\breve{k}$ is a unit vector in the wave propagation direction. The wavenumber contains information on the phase velocity dispersion and attenuation of the wave due to the Biot's global fluid flow.

From Eqs. A3 and A4 it is possible to show that

$$
\begin{aligned}
&\nabla(\nabla\cdot\mathbf{u}) = \big(-Ae^{i(\omega t-\mathbf{k}.\mathbf{r})}\mathbf{k}\cdot\breve{u}\big)\mathbf{k},\\
&\nabla(\nabla\cdot\mathbf{w}) = \big(-Be^{i(\omega t-\mathbf{k}.\mathbf{r})}\mathbf{k}\cdot\breve{w}\big)\mathbf{k},\\
&\nabla\times(\nabla\times\mathbf{u}) = -Ae^{i(\omega t-\mathbf{k}.\mathbf{r})}\mathbf{k}\times(\mathbf{k}\times\breve{u}).
\end{aligned}
\tag{A5}
$$

Introducing Eqs. A5 in the equations of motion (Eqs. 4), we get the following system of equations

$$
\begin{aligned}
0 =&\big(-\rho_b\breve{u} + H_U(\frac{k}{\omega})^2(\breve{k}\cdot\breve{u})\breve{k} - \mu(\frac{k}{\omega})^2\breve{k}\times(\breve{k}\times\breve{u})\big)A\\
&+\big(-\rho_f\breve{w} + \alpha M(\frac{k}{\omega})^2(\breve{k}\cdot\breve{w})\breve{k}\big)B,\\
0 =&\big(-\rho_f\breve{u} + \alpha M(\frac{k}{\omega})^2(\breve{k}\cdot\breve{u})\breve{k}\big)A\\
&+\big(-g\breve{w} + \frac{ib}{\omega}\breve{w} + M(\frac{k}{\omega})^2(\breve{k}\cdot\breve{w})\breve{k}\big)B.
\end{aligned}
\tag{A6}
$$

The solutions for this system of equation will depend on the relations between the vectors $\breve{k}$, $\breve{u}$, and $\breve{w}$. From the analysis performed by Pride et al. (1992), regardless the wave, there are no plane waves with $\breve{u}\neq\breve{w}$, because we would obtain the trivial solution $A = B = 0$ from Eqs. A6.

In the case of S-waves, the vectors $\breve{u}$ and $\breve{w}$ are parallel but are orthogonal to $\breve{k}$. Hence,

$$
\begin{aligned}
&(\breve{k}\cdot\breve{u}) = (\breve{k}\cdot\breve{w}) = 0,\\
&\breve{k}\times(\breve{k}\times\breve{u}) = -\breve{u}.
\end{aligned}
\tag{A7}
$$

And thus Eqs. A6 reduce to

$$
\begin{aligned}
&\big(-\rho_b + \mu(\frac{k}{\omega})^2\big)A - \rho_f B = 0,\\
&-\rho_f A + \big(-g + \frac{ib}{\omega}\big)B = 0.
\end{aligned}
\tag{A8}
$$

This homogeneous linear system of equations has non-trivial solutions only when the determinant is equal to zero. This condition yields the solution for the complex wavenumber for the S-wave in homogeneous media

$$
k(\omega) = \pm\left(\frac{\omega^2}{\mu}\left(\rho_b - \frac{\rho_f^2}{g(\omega) - \frac{ib(\omega)}{\omega}}\right)\right)^{\frac{1}{2}}.
\tag{A9}
$$

We have two possible solutions for $k(\omega)$. We chose the one with positive real component and negative imaginary component. To justify this, we consider a wave propagating in the direction of the x-axis

$$\begin{aligned}\mathbf{u} &= Ae^{\Im(k)x}e^{i(\omega t-\Re(k)x)}\breve{u},\\ \mathbf{w} &= Be^{\Im(k)x}e^{i(\omega t-\Re(k)x)}\breve{w}.\end{aligned} \tag{A10}$$

From this, it is straightforward to observe that the physically meaningful solution for the wavenumber satisfies $\Re(k) > 0$ and $\Im(k) < 0$ and that only one of the two solutions satisfies these conditions. Moreover, the phase velocity $V(\omega)$ of the medium can be defined as

$$V(\omega) = \frac{\omega}{\Re(k(\omega))}. \tag{A11}$$

By using Eq. A4 and the physically meaningful solution of Eq. A9, we compute the wavenumber and, thus, $V_S(\omega)$. We obtain the low-frequency limit velocity to be used in the elastic model from Eq. A11

$$V_S^{elas} = \lim_{\omega\to 0} V_S(\omega) = \sqrt{\frac{\mu}{\rho_b}}. \tag{A12}$$

For compressional waves, the wavenumber's direction is parallel to the direction of the solid and fluid displacements, hence

$$(\breve{k}\cdot\breve{u}) = (\breve{k}\cdot\breve{w}) = 1, \tag{A13a}$$

$$\breve{k}\times(\breve{k}\times\breve{u}) = 0. \tag{A13b}$$

Using these conditions in Eqs. A6, we get

$$(-\rho_b + H_U(\frac{k}{\omega})^2)A + (-\rho_f + \alpha M(\frac{k}{\omega})^2)B = 0, \tag{A14a}$$

$$(-\rho_f + \alpha M(\frac{k}{\omega})^2)A + (-g + \frac{ib}{\omega} + M(\frac{k}{\omega})^2)B = 0. \tag{A14b}$$

As for S-waves, the determinant of the system of equations must be zero to obtain nontrivial solutions. Imposing this condition leads to

$$ak^4 + bk^2 + c = 0, \tag{A15}$$

where

$$
\begin{aligned}
a &= (H_U M - \alpha^2 M^2)/\omega^4, \\
b &= (\frac{iH_U b(\omega)}{\omega} - H_U g(\omega) - \rho_b M + 2\rho_f M\alpha)/\omega^2, \\
c &= \rho_b g(\omega) - \frac{i\rho_b b(\omega)}{\omega} - \rho_f^2.
\end{aligned}
\tag{A16}
$$

This biquadratic equation has four solutions

$$
k_{1,2} = \pm\sqrt{k_+^2}, \tag{A17a}
$$

$$
k_{3,4} = \pm\sqrt{k_-^2}, \tag{A17b}
$$

where k_+^2 and k_-^2 are the solutions of the corresponding quadratic equation if we substitute $q = k^2$ in Eq. A15. Even though the four solutions are mathematically valid, only two of them are physically acceptable. Using the same criteria as for S-waves leads to the two solutions for P-waves. The fast and slow P-wave solutions are defined such that $V_{P_1}(\omega) > V_{P_2}(\omega)$.

Finally, the low-frequency limit velocity for the elastic model is given by

$$
V_P^{elas} = \lim_{\omega \to 0} V_{P_1}(\omega) = \sqrt{\frac{\lambda + 2\mu}{\rho_b}}. \tag{A18}
$$

In $\mathbb{R}^2$ and for the system of reference chosen, $\mathbf{k}$ is a complex wave vector such that $\mathbf{k}_j = (n_j, l_j)$, with $j = P_1, P_2, S$. In this case, the solutions of the plane wave analysis give the complex magnitude k whose real and imaginary components will satisfy the criteria mentioned above. Therefore both n and l will also fulfil the criteria.

APPENDIX B: SYSTEM OF EQUATIONS FOR A POROELASTIC THIN-LAYER MODEL

In the Methodology Section we showed that 6 boundary conditions must be set up for each fracture surface

$$u_x^{\Omega_1}(x,0,\omega) = u_x^{\Omega_2}(x,0,\omega), \tag{B1a}$$

$$u_y^{\Omega_1}(x,0,\omega) = u_y^{\Omega_2}(x,0,\omega), \tag{B1b}$$

$$w_y^{\Omega_1}(x,0,\omega) = w_y^{\Omega_2}(x,0,\omega), \tag{B1c}$$

$$p_f^{\Omega_1}(x,0,\omega) = p_f^{\Omega_2}(x,0,\omega), \tag{B1d}$$

$$\tau_{xy}^{\Omega_1}(x,0,\omega) = \tau_{xy}^{\Omega_2}(x,0,\omega), \tag{B1e}$$

$$\tau_{yy}^{\Omega_1}(x,0,\omega) = \tau_{yy}^{\Omega_2}(x,0,\omega), \tag{B1f}$$

$$u_x^{\Omega_2}(x,h,\omega) = u_x^{\Omega_3}(x,h,\omega), \tag{B1g}$$

$$u_y^{\Omega_2}(x,h,\omega) = u_y^{\Omega_3}(x,h,\omega), \tag{B1h}$$

$$w_y^{\Omega_2}(x,h,\omega) = w_y^{\Omega_3}(x,h,\omega), \tag{B1i}$$

$$p_f^{\Omega_2}(x,h,\omega) = p_f^{\Omega_3}(x,h,\omega), \tag{B1j}$$

$$\tau_{xy}^{\Omega_2}(x,h,\omega) = \tau_{xy}^{\Omega_3}(x,h,\omega), \tag{B1k}$$

$$\tau_{yy}^{\Omega_2}(x,h,\omega) = \tau_{yy}^{\Omega_3}(x,h,\omega). \tag{B1l}$$

Using Eqs. B1a, B1g, Eq. 6 and the fact that the incident fast P-wave is assumed to be homogeneous, it can be verified that

$$\begin{gathered} n_{P_1}^I = k_{P_1}^I sin(\theta_{P_1}^I) = n_j^q, \\ \text{for } \ q = R, U, D, T \ \text{ and } \ j = P_1, P_2, S. \end{gathered} \tag{B2}$$

This is the generalized Snell's law for a thin-layer model (Rubino et al., 2006) and allows us to determine the components of the wave vector for each type of wave as functions of the incidence angle.

Using Snell's law (Eq. B2), the boundary conditions (Eqs. B1) and the linear relation between the potential amplitudes corresponding to the relative fluid displacement and to the solid displacement field

$$\gamma^{\Omega_i} = B_j^{\Omega_i}/A_j^{\Omega_i}, \quad j = P_1, P_2, S, \tag{B3}$$

which can be computed from Eqs. A6, yield the following 12×12 linear system of equations whose solution provides the set of wave amplitudes as a function of frequency and incidence angle

$$\begin{aligned} nA_{P_1}^I =& - nA_{P_1}^R - nA_{P_2}^R - l_S^{\Omega_1} A_S^R + nA_{P_1}^U + nA_{P_2}^U + l_S^{\Omega_2} A_S^U \\ &+ nA_{P_1}^D + nA_{P_2}^D - l_S^{\Omega_2} A_S^D, \end{aligned} \tag{B4}$$

$$(u_x^{\Omega_1} = u_x^{\Omega_2} \ \text{at} \ \Gamma_1)$$

$$\begin{aligned} l_{P_1}^{\Omega_1} A_{P_1}^I =& l_{P_1}^{\Omega_1} A_{P_1}^R + l_{P_2}^{\Omega_1} A_{P_2}^R - nA_S^R - l_{P_1}^{\Omega_2} A_{P_1}^U - l_{P_2}^{\Omega_2} A_{P_2}^U \\ &+ nA_S^U + l_{P_1}^{\Omega_2} A_{P_1}^D + l_{P_2}^{\Omega_2} A_{P_2}^D + nA_S^D, \end{aligned} \tag{B5}$$

$$(u_y^{\Omega_1} = u_y^{\Omega_2} \ \text{at} \ \Gamma_1)$$

$$\begin{aligned} a_{P_1}^{\Omega_1} A_{P_1}^I =& a_{P_1}^{\Omega_1} A_{P_1}^R + a_{P_2}^{\Omega_1} A_{P_2}^R - b_S^{\Omega_1} A_S^R - a_{P_1}^{\Omega_2} A_{P_1}^U - a_{P_2}^{\Omega_2} A_{P_2}^U \\ &+ b_S^{\Omega_2} A_S^U + a_{P_1}^{\Omega_2} A_{P_1}^D + a_{P_2}^{\Omega_2} A_{P_2}^D + b_S^{\Omega_2} A_S^D, \end{aligned} \tag{B6}$$

$$(w_y^{\Omega_1} = w_y^{\Omega_2} \ \text{at} \ \Gamma_1)$$

$$\begin{aligned} -f_{P_1}^{\Omega_1} A_{P_1}^I =& f_{P_1}^{\Omega_1} A_{P_1}^R + f_{P_2}^{\Omega_1} A_{P_2}^R - f_{P_1}^{\Omega_2} A_{P_1}^U - f_{P_2}^{\Omega_2} A_{P_2}^U \\ &- f_{P_1}^{\Omega_2} A_{P_1}^D - f_{P_2}^{\Omega_2} A_{P_2}^D, \end{aligned} \tag{B7}$$

$$(p_f^{\Omega_1} = p_f^{\Omega_2} \ \text{at} \ \Gamma_1)$$

$$\begin{aligned} g_{P_1}^{\Omega_1} A_{P_1}^I =& g_{P_1}^{\Omega_1} A_{P_1}^R + g_{P_2}^{\Omega_1} A_{P_2}^R + c_S^{\Omega_1} A_S^R - g_{P_1}^{\Omega_2} A_{P_1}^U \\ &- g_{P_2}^{\Omega_2} A_{P_2}^U - c_S^{\Omega_2} A_S^U + g_{P_1}^{\Omega_2} A_{P_1}^D \\ &+ g_{P_2}^{\Omega_2} A_{P_2}^D - c_S^{\Omega_2} A_S^D, \end{aligned} \tag{B8}$$

$$(\tau_{xy}^{\Omega_1} = \tau_{xy}^{\Omega_2} \ \text{at} \ \Gamma_1)$$

$$\begin{aligned} h_{P_1}^{\Omega_1} A_{P_1}^I =& - h_{P_1}^{\Omega_1} A_{P_1}^R - h_{P_2}^{\Omega_1} A_{P_2}^R + g_S^{\Omega_1} A_S^R + h_{P_1}^{\Omega_2} A_{P_1}^U \\ &+ h_{P_2}^{\Omega_2} A_{P_2}^U - g_S^{\Omega_2} A_S^U + h_{P_1}^{\Omega_2} A_{P_1}^D + h_{P_2}^{\Omega_2} A_{P_2}^D \\ &+ g_S^{\Omega_2} A_S^D, \end{aligned} \tag{B9}$$

$$(\tau_{yy}^{\Omega_1} = \tau_{yy}^{\Omega_2} \ \text{at} \ \Gamma_1)$$

$$\begin{aligned}0 =& - ne^{il_{P_1}^{\Omega_2}h}A_{P_1}^U - ne^{il_{P_2}^{\Omega_2}h}A_{P_2}^U - l_S^{\Omega_2}e^{il_S^{\Omega_2}h}A_S^U \\ & -ne^{-il_{P_1}^{\Omega_2}h}A_{P_1}^D - ne^{-il_{P_2}^{\Omega_2}h}A_{P_2}^D + l_S^{\Omega_2}e^{-il_S^{\Omega_2}h}A_S^D \\ & +ne^{-il_{P_1}^{\Omega_3}h}A_{P_1}^T + ne^{-il_{P_2}^{\Omega_3}h}A_{P_2}^T - l_S^{\Omega_3}e^{-il_S^{\Omega_3}h}A_S^T,\end{aligned} \tag{B10}$$

$(u_x^{\Omega_2} = u_x^{\Omega_3} \text{ at } \Gamma_2)$

$$\begin{aligned}0 =& l_{P_1}^{\Omega_2}e^{il_{P_1}^{\Omega_2}h}A_{P_1}^U + l_{P_2}^{\Omega_2}e^{il_{P_2}^{\Omega_2}h}A_{P_2}^U - ne^{il_S^{\Omega_2}h}A_S^U \\ & -l_{P_1}^{\Omega_2}e^{-il_{P_1}^{\Omega_2}h}A_{P_1}^D - l_{P_2}^{\Omega_2}e^{-il_{P_2}^{\Omega_2}h}A_{P_2}^D - ne^{-il_S^{\Omega_2}h}A_S^D \\ & +l_{P_1}^{\Omega_3}e^{-il_{P_1}^{\Omega_3}h}A_{P_1}^T + l_{P_2}^{\Omega_3}e^{-il_{P_2}^{\Omega_3}h}A_{P_2}^T + ne^{-il_S^{\Omega_3}h}A_S^T,\end{aligned} \tag{B11}$$

$(u_y^{\Omega_2} = u_y^{\Omega_3} \text{ at } \Gamma_2)$

$$\begin{aligned}0 =& a_{P_1}^{\Omega_2}e^{il_{P_1}^{\Omega_2}h}A_{P_1}^U + a_{P_2}^{\Omega_2}e^{il_{P_2}^{\Omega_2}h}A_{P_2}^U - b_S^{\Omega_2}e^{il_S^{\Omega_2}h}A_S^U \\ & -a_{P_1}^{\Omega_2}e^{-il_{P_1}^{\Omega_2}h}A_{P_1}^D - a_{P_2}^{\Omega_2}e^{-il_{P_2}^{\Omega_2}h}A_{P_2}^D - b_S^{\Omega_2}e^{-il_S^{\Omega_2}h}A_S^D \\ & +a_{P_1}^{\Omega_3}e^{-il_{P_1}^{\Omega_3}h}A_{P_1}^T + a_{P_2}^{\Omega_3}e^{-il_{P_2}^{\Omega_3}h}A_{P_2}^T + b_S^{\Omega_3}e^{-il_S^{\Omega_3}h}A_S^T,\end{aligned} \tag{B12}$$

$(w_y^{\Omega_2} = w_y^{\Omega_3} \text{ at } \Gamma_2)$

$$\begin{aligned}0 =& f_{P_1}^{\Omega_2}e^{il_{P_1}^{\Omega_2}h}A_{P_1}^U + f_{P_2}^{\Omega_2}e^{il_{P_2}^{\Omega_2}h}A_{P_2}^U + f_{P_1}^{\Omega_2}e^{-il_{P_1}^{\Omega_2}h}A_{P_1}^D \\ & +f_{P_2}^{\Omega_2}e^{-il_{P_2}^{\Omega_2}h}A_{P_2}^D - f_{P_1}^{\Omega_3}e^{-il_{P_1}^{\Omega_3}h}A_{P_1}^T - f_{P_2}^{\Omega_3}e^{-il_{P_2}^{\Omega_3}h}A_{P_2}^T,\end{aligned} \tag{B13}$$

$(p_f^{\Omega_2} = p_f^{\Omega_3} \text{ at } \Gamma_2)$

$$\begin{aligned}0 =& g_{P_1}^{\Omega_2}e^{il_{P_1}^{\Omega_2}h}A_{P_1}^U + g_{P_2}^{\Omega_2}e^{il_{P_2}^{\Omega_2}h}A_{P_2}^U + c_S^{\Omega_2}e^{il_S^{\Omega_2}h}A_S^U \\ & -g_{P_1}^{\Omega_2}e^{-il_{P_1}^{\Omega_2}h}A_{P_1}^D - g_{P_2}^{\Omega_2}e^{-il_{P_2}^{\Omega_2}h}A_{P_2}^D + c_S^{\Omega_2}e^{-il_S^{\Omega_2}h}A_S^D \\ & +g_{P_1}^{\Omega_3}e^{-il_{P_1}^{\Omega_3}h}A_{P_1}^T + g_{P_2}^{\Omega_3}e^{-il_{P_2}^{\Omega_3}h}A_{P_2}^T - c_S^{\Omega_3}e^{-il_S^{\Omega_3}h}A_S^T,\end{aligned} \tag{B14}$$

$(\tau_{xy}^{\Omega_2} = \tau_{xy}^{\Omega_3} \text{ at } \Gamma_2)$

$$\begin{aligned}0 =& - h_{P_1}^{\Omega_2}e^{il_{P_1}^{\Omega_2}h}A_{P_1}^U - h_{P_2}^{\Omega_2}e^{il_{P_2}^{\Omega_2}h}A_{P_2}^U + g_S^{\Omega_2}e^{il_S^{\Omega_2}h}A_S^U \\ & -h_{P_1}^{\Omega_2}e^{-il_{P_1}^{\Omega_2}h}A_{P_1}^D - h_{P_2}^{\Omega_2}e^{-il_{P_2}^{\Omega_2}h}A_{P_2}^D - g_S^{\Omega_2}e^{-il_S^{\Omega_2}h}A_S^D \\ & +h_{P_1}^{\Omega_3}e^{-il_{P_1}^{\Omega_3}h}A_{P_1}^T + h_{P_2}^{\Omega_3}e^{-il_{P_2}^{\Omega_3}h}A_{P_2}^T + g_S^{\Omega_3}e^{-il_S^{\Omega_3}h}A_S^T,\end{aligned} \tag{B15}$$

$(\tau_{yy}^{\Omega_2} = \tau_{yy}^{\Omega_3} \text{ at } \Gamma_2)$

with

$$
\begin{aligned}
a_i^{\Omega_j} &= l_i^{\Omega_j}\gamma_i^{\Omega_j}, \\
b_S^{\Omega_j} &= n\gamma_S^{\Omega_j}, \\
c_S^{\Omega_j} &= \mu^{\Omega_j}[(l_S^{\Omega_j})^2 - n^2], \\
f_i^{\Omega_j} &= (k_i^{\Omega_j})^2 M^{\Omega_j}(\alpha^{\Omega_j} + \gamma_i^{\Omega_j}), \\
g_i^{\Omega_j} &= 2\mu^{\Omega_j} n l_i^{\Omega_j}, \\
h_i^{\Omega_j} &= 2\mu^{\Omega_j}(l_i^{\Omega_j})^2 + (k_i^{\Omega_j})^2[M^{\Omega_j}\alpha^{\Omega_j}\gamma_i^{\Omega_j} + \lambda^{\Omega_j}], \\
&\text{for } j = 1,2,3 \text{ and } i = P_1, P_2.
\end{aligned}
\tag{B16}
$$

From the solution of the system of equations given by Eqs. B4-B15 we obtain the amplitudes of the potentials, which allow us to compute the reflection coefficients.

APPENDIX C: ENERGY COEFFICIENTS

The poroelastic variables derived in Appendix B can be used to evaluate the energy coefficients. Rubino et al. (2006) present a formal generalization to the expression of the energy flux Umov-Poynting vector for a porous composite medium. Here, we proceed analogously, but we consider only one solid phase instead of the two solid phases involved in composite media. The general expression for the energy balance equation in the frequency domain remains the same

$$
i\omega\int_V 2(W-T)dV - \int_V (\hat{D}_W + \hat{D}_T)dV = \int_{\delta V} \mathbf{P}\cdot\nu dS, \tag{C1}
$$

where T and W are the kinetic and strain energy densities and $\hat{D}_T$ and $\hat{D}_W$ are the rates of dissipation of the corresponding energy densities over a volume V. δV represents the surface of V with outer normal ν. In this case, the complex Umov-Pointing vector $\mathbf{P}$ in Eq. C1 has components P_k equal to

$$
P_k(u,w) = -\frac{i\omega}{2}(\tau_{kj}(u_j)^* - p_f(w_k)^*), \qquad \text{for } k,j = x,y, \tag{C2}
$$

where the symbol $*$ denotes the complex conjugate and the sum convention is applied on the index j. Moreover, the real Umov-Poynting vector $\mathbf{P_R} = P_{Rk}\breve{e}_k$ with components

$$P_{Rk} = -(Re(\tau_{kj})Re(i\omega u_j) - Re(p_f)Re(i\omega w_k)), \tag{C3}$$

has continuous normal components at the interfaces Γ_1 and Γ_2 as a consequence of the boundary conditions (Eqs. B1). The time-average of the normal component of the energy flux is given by

$$F = \frac{\omega}{2\pi}\int_0^{\frac{2\pi}{\omega}} \mathbf{P_R}\cdot\breve{e}_y dt = \frac{\omega}{2\pi}\int_0^{\frac{2\pi}{\omega}} P_{Ry} dt, \tag{C4}$$

and it represents the magnitude and direction of the time-averaged power flow. Applying the superposition principle, F can be split into different components associated with the different wave modes present in each part of the medium. Hence, the partial orthodox fluxes $F_{k,k}$ (same Biot wave mode) are defined as

$$\begin{aligned} F_{k,k} =& \frac{\omega}{2\pi}\int_0^{\frac{2\pi}{\omega}} -[Re(\tau_{yj,k})Re(i\omega u_{j,k}) \\ & - Re(p_{f,k})Re(i\omega w_{y,k})]dt, \qquad \text{for } j = x, y. \end{aligned} \tag{C5}$$

And the interference fluxes $F_{k,q}$ (mixed Biot wave modes) are given by

$$\begin{aligned} F_{k,q} =& \frac{\omega}{2\pi}\int_0^{\frac{2\pi}{\omega}} -(Re(\tau_{yj,k})Re(i\omega u_{j,q}) \\ & + Re(\tau_{yj,q})Re(i\omega u_{j,k}) \\ & - Re(p_{f,k})Re(i\omega w_{y,q}) \\ & - Re(p_{f,q})Re(i\omega w_{y,k}))dt, \qquad \text{for } j = x, y \end{aligned} \tag{C6}$$

where $k, q = I_{P_1}, R_{P_1}, R_{P_2}, R_S$ in Ω_1, $k, q = L_{P_1}, L_{P_2}, L_S$ in Ω_2, and $k, q = T_{P_1}, T_{P_2}, T_S$ in Ω_3 denote the wave associated with the variable and the sum convention is applied on the index j. The symbols L_j refer to the variables computed using the upgoing and downgoing waves within the fracture.

The energy balance written in terms of the interference and orthodox fluxes result

$$\begin{aligned} F_{I,P_1} = & - F_{R_{P_1},R_{P_1}} - F_{R_{P_2},R_{P_2}} - F_{R_S,R_S} \\ & - F_{R_{P_1},R_{P_2}} - F_{R_{P_2},R_S} - F_{R_{P_1},R_S} \\ & + F_{L_{P_1},L_{P_1}} + F_{L_{P_2},L_{P_2}} + F_{L_S,L_S} \\ & + F_{L_{P_1},L_{P_2}} + F_{L_{P_2},L_S} + F_{L_{P_1},L_S}, \qquad \text{at } \Gamma_1 \end{aligned} \tag{C7a}$$

$$\begin{aligned} & F_{F_{P_1},F_{P_1}} + F_{F_{P_2},F_{P_2}} + F_{F_S,F_S} + F_{F_{P_1},F_{P_2}} + F_{F_{P_2},F_S} \\ & + F_{F_{P_1},F_S} = F_{T_{P_1},T_{P_1}} + F_{T_{P_2},T_{P_2}} + F_{T_S,T_S} \\ & + F_{T_{P_1},T_{P_2}} + F_{T_{P_2},T_S} + F_{T_{P_1},T_S}, \qquad \text{at } \Gamma_2 \end{aligned} \tag{C7b}$$

where

$$F_{I,P_1} = F_{I_{P_1},I_{P_1}} + F_{I_{P_1},R_{P_1}} + F_{I_{P_1},R_{P_2}} + F_{I_{P_1},R_s}, \tag{C8}$$

is the incident energy flux for P_1 incidence. Finally, from these fluxes it is possible to define the energy reflection and transmission coefficients as

$$\begin{aligned} ER_{P_1,j} &= \frac{F_{Rj,Rj}}{F_{I,P_1}}, \\ ET_{P_1,j} &= \frac{F_{Tj,Tj}}{F_{I,P_1}}, \qquad j = P_1, P_2, S. \end{aligned} \tag{C9}$$

REFERENCES

Biot, M. A. (**1962**). "Mechanics of deformation and acoustic propagation in porous media," J. Appl. Phys. **33**, 1482–1498.

Brajanovski, M., Müller T. M., and Gurevich, B. (**2006**). "Characteristic frequencies of seismic attenuation due to wave-induced fluid flow in fractured porous media," Geophys. J. Int. **166**, 574–578.

Coates, R. T., and Schoenberg, M. (**1995**). "Finite-difference modeling of faults and fractures," Geophysics **60**, 1514–1526.

Dutta, N. C., and Ode, H. (**1983**). "Seismic reflections from a gas-water contact," Geophysics **48**, 148–162.

Gassmann, F. (**1951**). “Elastic waves through a packing of spheres,” Geophysics **16**, 673–685.

Gurevich, B., Marschall, R., and Shapiro, S. A. (**1994**). “Effect of fluid flow on seismic reflections from a thin layer in a porous medium,” J. Seism. Explor. **3**, 125–140.

Gurevich, B., Schoenberg, M. (**1999**). “Interface conditions for Biot’s equations of poroelasticity,” J. Acoust. Soc. Am. **105**, 2585–2589.

Gurevich, B., Brajanovski, M., Galvin, R. J., Müller, T. M., and Toms-Stewart, J. (**2009**). “P-wave dispersion and attenuation in fractured and porous reservoirs-poroelasticity approach,” Geophys. Prospect. **57**, 225–237.

Hudson, J. A., and Liu, E. (**1999**). “Effective elastic properties of heavily faulted structures,” Geophysics **64**, 479–485.

Johnson, D.L., Koplik, J., and Dashen, R. (**1987**). “Theory of dynamic permeability and tortuosity in fluid-saturated porous media,” J. Fluid Mech. **176**, 379-402.

Li, J. C., Li, H. B., Jiao, Y.Y., Liu, Y.Q., Xia, X., and Yu, C. (**2014**). “Analysis for oblique wave propagation across filled joints based on thin-layer interface model,” J. Appl. Geophys. **102**, 39–46.

Minato, S., and Ghose R. (**2014**). “Imaging and characterization of a subhorizontal nonwelded interface from point source elastic scattering response,” Geophys. J. Int. **197**, 1090–1095.

Müller, T. M., and Rothert, E. (**2006**). “Seismic attenuation due to waveinduced flow: Why Q in random structures scales differently,” Geophys. Res. Lett. **33**, L16305.

Müller, T. M., Gurevich, B., and Lebedev, M. (**2010**). “Seismic wave attenuation and dispersion resulting from wave-induced flow in porous rocks: A review,” Geophysics **75**, 147–164.

Nakagawa, S., and Schoenberg, M. A. (**2007**). “Poroelastic modeling of seismic boundary conditions across a fracture,” J. Acoust. Soc. Am. **122**, 831–847.

Oelke, A., Alexandrov, D., Abakumov, I., Glubokovskikh, S., Shigapov, R., Krüger, O. S., Kashtan, B., Troyan, V., and Shapiro, S. A. (**2013**). “Seismic reflectivity of hydraulic fractures approximated by thin fluid layers," Geophysics **78**, 79–87.

Pirak-Nolte, L. J., Myer, L. R., and Cook, N. G. W. (**1990**). "Transmission of seismic waves across single natural fractures," J. Geophys. Res. **95**, 8617–8638.

Pride, S., Gangi, A., and Dale Morgan, F. (**1992**). "Deriving the equations of motion for porous isotropic media," J. Acoust. Soc. Am. **92**, 3278–3290.

Rubino, J. G., Ravazzoli, C. L., and Santos, J. E. (**2006**). "Reflection and transmission of waves in composite porous media: A quantification of energy conversions involving slow waves," J. Acoust. Soc. Am. **120**, 2425–2436.

Rubino, J. G., Müller, T. M., Guarracino, L., Milani, M., and Holliger, K. (**2014**). "Seismoacoustic signatures of fracture connectivity," J. Geophys. Res.: Solid Earth. **119**, 2252–2271.

Rubino, J. G., Castromán, G. A., Müller, T. M., Monachesi, L. B., Zyserman, F. I., and Holliger, K. (**2015**). "Including poroelastic effects in the linear slip theory," Geophysics **80**, A51–A56.

Schoenberg, M. A. (**1980**). "Elastic wave behavior across linear slip interfaces," J. Acoust. Soc. Am. **68**, 1516–1521.

Worthington, M. H., and Lubbe, R. (**2007**). "The scaling of fracture compliance," Geological Society (London) Special Publications. **270**, 73–82.

TABLE I. Material properties of the reference model considered in this study.

Property	**Background**	**Fracture**
Grain bulk modulus K_s [GPa]	36	36
Grain density ρ_s [g/cm^3]	2.7	2.7
Porosity ϕ	0.15	0.8
Frame bulk modulus K_m [GPa]	9	0.056
Frame shear modulus μ_m [GPa]	7	0.033
Permeability κ [D]	0.1	100
Tortuosity S	3	1
Thickness h [m]	-	0.001
Fluid density ρ_f [g/cm^3]	1	
Fluid bulk modulus K_f [GPa]	2.25	
Fluid viscosity η [Poise]	0.01	

LIST OF FIGURES